Progress in Tandem Solar Cells Based on Hybrid Organic–Inorganic Perovskites

*Bo Chen, Xiaopeng Zheng, Yang Bai, Nitin P. Padture, and Jinsong Huang**

Owing to their high efficiency, low-cost solution-processability, and tunable bandgap, perovskite solar cells (PSCs) made of hybrid organic-inorganic perovskite (HOIP) thin films are promising top-cell candidates for integration with bottom-cells based on Si or other low-bandgap solar-cell materials to boost the power conversion efficiency (PCE) beyond the Shockley-Quiesser (S-Q) limit. In this review, recent progress in such tandem solar cells based on the emerging PSCs is summarized and reviewed critically. Notable achievements for different tandem solar cell configurations including mechanically-stacked, optical coupling, and monolithically-integrated with PSCs as top-cells are described in detail. Highly-efficient semitransparent PSC top-cells with high transmittance in near-infrared (NIR) region are critical for tandem solar cells. Different types of transparent electrodes with high transmittance and low sheet-resistance for PSCs are reviewed, which presents a grand challenge for PSCs. The strategies to obtain wide-bandgap PSCs with good photostability are discussed. The PCE reduction due to reflection loss, parasitic absorption, electrical loss, and current mismatch are analyzed to provide better understanding of the performance of PSC-based tandem solar cells.

1. Introduction

The development of solar cells for clean and renewable energy has been driven by the reduction of levelized cost of electricity (LCOE). Increasing the power conversion efficiency (PCE) of solar panels not only generates more electricity but also reduces the associated cost such as shipment, installation, land usage, etc., contributing to LCOE reduction. Si-based solar cells have dominated the terrestrial solar panel market with an average panel PCE of around 20%, while the record cell efficiency stands at 25.6%, which is very close to the Shockley-Quiesser (S-Q) limit of single-junction solar cells.[1] Thin-film solar cells based on copper indium gallium selenide (CIGS) and cadmium telluride (CdTe) have seen rapid development over the past two decades, with record PCE of 22.3% and 22.1%, respectively.[1] However, due to the below-bandgap absorption loss and the thermal-relaxation loss of hot charge-carriers (**Figure 1**a), the PCE of single-junction solar cells cannot exceed the S-Q limit.[2,3] Integrating low-cost and high-efficiency wide-bandgap top solar cells with low-bandgap (e.g., Si, CIGS, CdTe, etc.) bottom solar cells to form tandem solar cells is clearly a promising strategy for improving the photovoltaic (PV) performance beyond the S-Q limit. The tandem configurations allow the high-energy photons to be absorbed in the top-cell, which generates high voltage to reduce the thermalization loss, and also allows the bottom-cell to absorb the transmitted low-energy photons, which leads to broader harvesting of the solar spectrum (Figure 1b).

Si-based solar cells dominate the world photovoltaics market, with ≈53 GW capacity installed in 2015.[4,5] This makes them an excellent candidate for bottom-cells in tandem solar cell structures, with other wide-bandgap solar cells as top-cells, without significant additional capital expense. In addition, the low bandgap of Si (1.1 eV) is almost ideal for two-junction tandem solar cells to achieve PCE above 30%. The grand challenge for tandem solar cells is to find a low-cost and high-efficiency wide-bandgap top-cell. Based on simulations, >30% PCE can be achieved if 1.70–1.85 eV bandgap top-cell is combined with Si bottom-cell.[3,6,7] Several pathways for unifying the high-efficiency merits of III-V semiconductor solar cells with the Si bottom-cell have been explored.[8,9] However, they have met with limited success to-date, primarily because the lattice and thermal-expansion-coefficient mismatches make it difficult to grow of III-V materials on Si substrate,[10,11] in addition to the potential high cost associated with the vacuum-based film growth of III-V materials. This situation has changed recently with the development of perovskite solar cells (PSCs) based on solution-processed hybrid organic-inorganic perovskite (HOIP) thin films which can be easily deposited on to Si solar cells without the need of lattice matching.

The emerging HOIPs have several distinct advantages as the candidates for top-cells in a tandem solar cell architecture with Si as the bottom-cells. First of all, high-PCE PSCs (with certified record efficiency as high as 22.1%) have been achieved in a relatively short period of time.[12–18] The HOIP materials possess extraordinary optoelectronic properties for PV active layer application, including strong absorption, large carrier mobility, long carrier recombination lifetime, long carrier diffusion length

Dr. B. Chen, X. Zheng, Dr. Y. Bai, Prof. J. Huang
Department of Mechanical and Materials Engineering
University of Nebraska-Lincoln
Lincoln, NE 68588, USA
E-mail: jhuang2@unl.edu
Prof. N. P. Padture
School of Engineering
Brown University
Providence, RI 02912, USA

DOI: 10.1002/aenm.201602400

(longer than the optical absorption length), defect tolerance, intrinsic semiconductor, etc.[19–23] More details about the fundamental properties of HOIP materials can be found in other review papers.[24,25] Second, the materials are earth-abundant and low-cost; they can also be recovered from other industrial materials and products.[26] Third, one distinct advantage of using HOIPs for tandem solar cells with other thin-film technologies is that the HOIP thin films can be easily fabricated on various substrates without the need for lattice matching, owing to the 'softness' of these materials and their defects-tolerance. Fourth, they can be deposited by low-temperature processes such as spin-coating, doctor-blading, slot-die coating, dip-coating, thermal evaporation, etc., which minimize the damage to the bottom-cell.[27–32] Finally, the bandgap of HOIP light-absorber can be tuned in the range 1.17–3.10 eV through compositional engineering, although it is challenging to stabilize some HOIP materials with bandgap >1.65 eV.[33–36] Almansouri et al.[37,38] have predicted that a practical PCE of ≈30% in dual-junction, two-terminal PSC/Si tandem solar cells is achievable.

Despite the significant challenges in the integration of the PSCs directly with other solar cells, significant progress has been made in the past few years, which highlights the promise of PSCs in tandem solar cell application. As shown in Figure 1c, tandem solar cells can be structured as two-terminal configuration with top-cell and bottom-cell connected in series or mechanically-stacked or optically-coupled four-terminal configuration with top-cell and bottom-cell operated separately. This article reviews the progress of PSC-based tandem solar cells with dissimilar active layers, including PSC/Si, PSC/CIGS, and PSC-1/PSC-2 tandem structures. To date, three different tandem configurations based on the integration of PSC top-cell with Si bottom-cell, CIGS bottom-cell, and other PSC bottom-cells have been investigated, and the details are presented in Section 2. The recent studies on transparent electrodes for the PSC top-cells are reviewed in Section 3. Considering the optimum bandgap of the top-cells with Si bottom-cell is 1.70–1.85 eV, many studies have focused on high-efficiency and stable wide-bandgap PSCs for tandem application, which are reviewed in Section 4. Finally, power losses in the tandem solar cells due to reflection loss, parasitic absorption, and electrical loss are discussed in Section 5.

2. Tandem Configurations

2.1. Mechanically-Stacked Four-Terminal Devices

Mechanical stacking of a PSC top-cell on top of a Si or a CIGS bottom-cell for a four-terminal tandem device allows processing flexibility and provides some unique advantages. Since the top-cell and the bottom-cell are fabricated independently in this case, each sub-cell can be fabricated using their optimized processes without any additional processing restrictions. Moreover, PSCs can serve as an add-on device to commercial Si-based solar cells to further improve their PCE. Typically, the as-deposited transparent electrodes for the semi-transparent PSCs have slightly lower transmittance than the bottom transparent conducting oxide (TCO)/glass substrate. Therefore, the semitransparent PSCs show higher PCE under illumination from the glass side compared to illumination from the deposited-transparent-electrode side. Therefore, mechanically-stacked tandem solar cells can utilize the best performance of the semitransparent PSCs through illumination from the TCO/glass side to minimize the current loss at the transparent electrode, and to allow a large processing window.

The PV parameters of mechanically-stacked four-terminal tandem solar cells with PSCs as the top-cell are summarized in **Table 1**. The first prototype of mechanically-stacked PSC/CIGS and PSC/Si four-terminal tandem devices was reported by Bailie et al.[39] in 2014 (**Figure 2**a). They utilized a Ag nanowire

Bo Chen is a postdoctoral research associate in Department of Mechanical and Materials Engineering at University of Nebraska-Lincoln. He received his Ph.D. degree in Materials Science and Engineering from Virginia Tech in 2012. His recent research focuses on perovskite solar cells and perovskite/Si tandem cells.

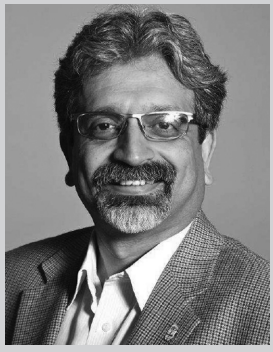

Nitin P. Padture is the Otis E. Randall University Professor (designate) in the School of Engineering and Director of Institute for Molecular and Nanoscale Innovation at Brown University. Previously he was College of Engineering Distinguished Professor at the Ohio State University (OSU), and also the founding Director of the National Science Foundation funded Materials Research Science & Engineering Center at OSU. His research interests are in advanced structural ceramics and functional nanomaterials, with applications ranging from jet engines to nanoelectronic devices to solar cells.

Jinsong Huang received his Ph.D. degree in Material Science and Engineering from the University of California—Los Angeles in 2007. He is now the Susan J. Rosowski Professor in the Department of Mechanical Engineering at University of Nebraska—Lincoln (UNL). His current research interests include solution processed electronic materials for applications in sensing, energy and consumer electronics.

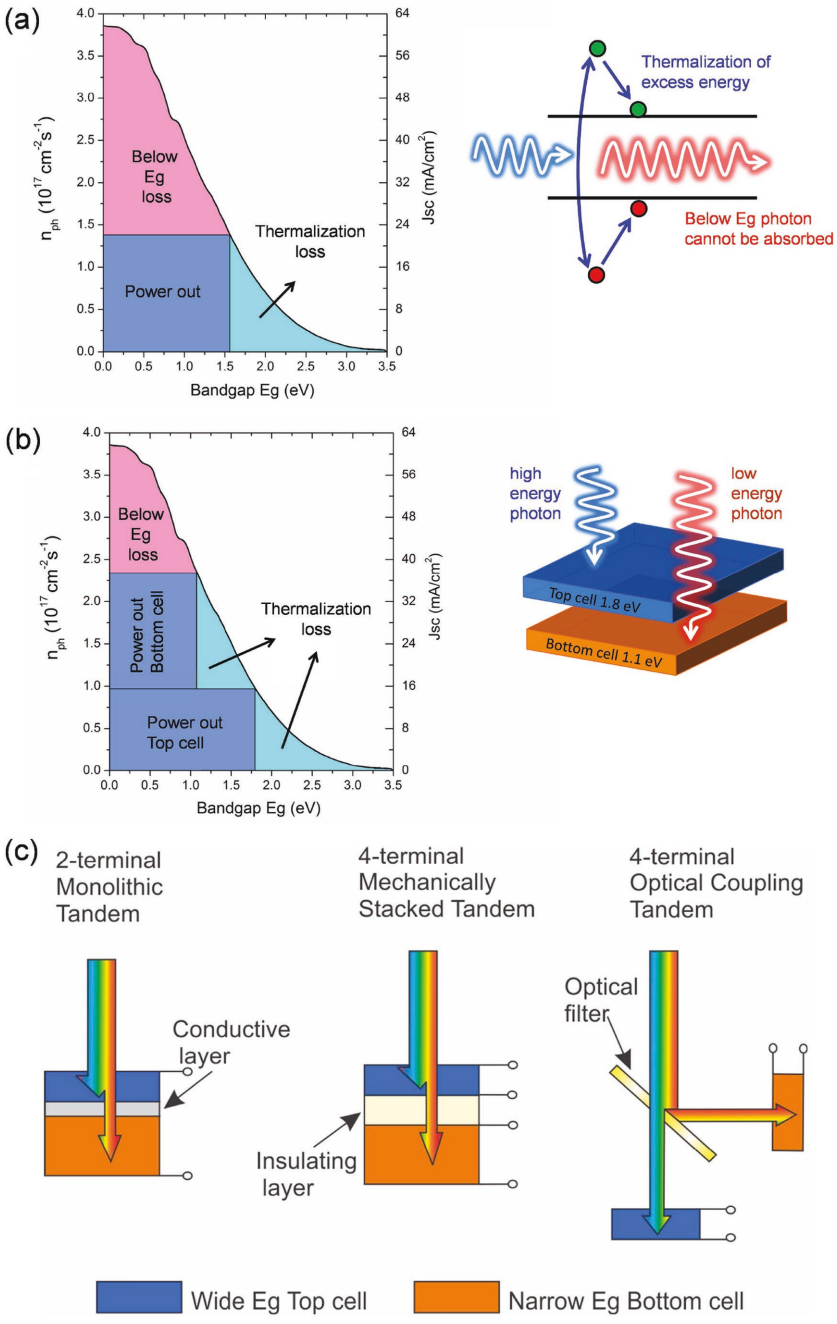

Figure 1. Thermalization loss and below-E_g loss of a) a single-junction solar cell with E_g of 1.55 eV and b) dual-junction tandem solar cell with 1.8-eV E_g top-cell and 1.1-eV E_g bottom-cell. The relation between the absorbed photon flux n_{ph} and the bandgap E_g of light absorber is obtained from Ref. [2]. Adapted with permission.[2] Copyright 1980, AIP Publishing. c) Three common tandem configurations with the colored arrows showing how the solar spectrum is transmitted and absorbed by the top and the bottom cells. Adapted with permission.[3] Copyright 2016, Nature Publishing Group.

(AgNW) mesh as the transparent electrode for the PSC top-cell, which resulted in a semitransparent PSC with a PCE of 12.7%, and 60–77% transmittance in the wavelength range from 800 nm to 1200 nm. When a CIGS solar cell with a PCE of 17.0% was used as the bottom-cell underneath the semitransparent PSC, the short-circuit current density (J_{SC}) reduced from 31.2 mA cm^{-2} to 10.9 mA cm^{-2}, and the open-circuit voltage (V_{OC}) decreased from 0.771 V to 0.682 V because of the attenuated sunlight available to the CIGS bottom-cell (Figure 2b). This resulted in a PCE of 5.9% for the filtered CIGS bottom-cell, and a total PCE of 18.6% for the tandem solar cell. Werner, Löper and co-workers introduced sputtered TCO in the semitransparent PSC top-cell, and they obtained 13.4% PCE for the semitransparent PSCs with 10 nm MoO_x/120 nm indium zinc oxide (IZO) as the transparent electrode.[40,41,45] The filtered Si heterojunction (SHJ) bottom-cell showed 9.38% PCE compared to 21.73% PCE for the un-filtered SHJ cell, which yielded a four-terminal tandem solar cell with 22.8% PCE.[45] When utilizing ultra-thin metal transparent-electrode for mechanically-stacked tandem solar cells, Yang et al.[42] improved the PCE of CIGS bottom-cell from 12.4% to 15.5% with the PSC/CIGS tandem structure.

Besides the investigation of PSC top-cells, Chen et al.[50] also reported enhancing the performance of Si bottom-cell in tandem configuration (Figure 2c). Considering that the Si bottom-cell is mainly responsible for NIR-light harvesting in the tandem solar cell, they fabricated an IR-enhanced SHJ cell by applying a double-layer antireflection coating on the front side and a MgF_2 back reflector layer on the back side to reduce parasitic absorption of NIR light. Because IZO has higher carrier-mobility than indium tin oxide (ITO), conventional sputtered-ITO was replaced by IZO as a lateral transport layer on the front side of the SHJ cell, which can decrease parasitic losses induced by free-carrier absorption. With MgF_2 reflector between Ag and Si at the back side of the SHJ cell, the fraction of light that reaches the lossy Ag reflector was reduced, thus suppressing the plasmonic absorption of light arriving outside of the transmission cone. A high PCE of 23.0% was achieved for the PSC/Si tandem solar cells based on the ultra-thin metal transparent electrode and NIR-enhanced Si bottom-cell (Figure 2d).[50] Similarly, Werner et al.[51] mechanically-stacked IR-enhanced SHJ cell with semitransparent PSC, with sputtered IO:H/ITO as the transparent electrode, and they obtained PCE as high as 25.2% for the 4-terminal PSC/Si tandem device.

Most of the reported PSC/Si and PSC/CIGS tandem devices involve $CH_3NH_3PbI_3$ ($MAPbI_3$) as the top-cell, which has a non-optimum bandgap of 1.55 eV. However, the optimum bandgap for top-cell is 1.70 eV–1.85 eV when integrating with Si bottom-cell.[3,6,7] McMeekin et al.[47] prepared a semitransparent PSC based on 1.74 eV bandgap photo-stable $FA_{0.83}Cs_{0.17}Pb(I_{0.6}Br_{0.4})_3$ active

Table 1. Summary of PV parameters for different mechanically-stacked four-terminal tandem devices based on PSC top-cells.

Device	V_{OC} [V]	J_{SC} [mA cm^{-2}]	*FF* [%]	*PCE* [%]	Total *PCE* [%]	ST-Electrode for PSC	Ref.
Top PSC	1.025	17.5	71.0	12.7	18.6	AgNW	[39]
Bottom CIGS cell	0.682	10.9	78.8	5.9			
Top PSC	1.025	17.5	71.0	12.7	17.0	AgNW	[39]
Bottom Si cell	0.547	11.1	70.4	4.3			
Top PSC	0.821	14.5	51.9	6.2	13.4	MoO_x/Sputtered ITO	[40]
Bottom SHJ cell	0.689	13.7	76.7	7.2			
Top PSC	0.87	17.5	68.0	10.36	18.18	MoO_x/Sputtered IZO	[41]
Bottom SHJ cell	0.69	14.6	77.6	7.82			
Top PSC	0.938	17.36	59.6	9.71	18.19	Sputtered IZO	[41]
Bottom SHJ cell	0.693	15.81	77.44	8.48			
Top PSC	1.05	14.6	75.1	11.5	15.5	MoO_x/(Au 1 nm&Ag 10 nm)/MoO_x	[42]
Bottom CIGS cell	0.56	10.2	69.6	4.0			
Top PSC	1.034	16.7	70.3	12.1	19.5	MoO_x/Sputtered ZnO:Al/MgF_2	[43]
Bottom CIGS cell	0.661	14.4	77.4	7.4			
Top PSC	0.90	12.6	55.0	6.2	13.2	graphene	[44]
Bottom SHJ cell	0.67	14.0	73.8	7.0			
Top PSC	1.03	19.0	68.5	13.4	22.8	MoO_x/Sputtered IZO	[45]
Bottom SHJ cell	0.702	17.0	78.6	9.38			
Top PSC	1.104	17.4	73.6	14.2	20.5	MoO_x/Sputtered In_2O_3:H	[46]
Bottom CIGS cell	0.667	12.7	74.9	6.3			
Top PSC	1.10	19.9	70.7	15.1	22.4	ITO buffer layer/Sputtered ITO	[47]
Bottom SHJ cell	0.69	13.9	76.4	7.3			
Top PSC	0.952	16.5	77.4	12.3	18.0	AZO/Sputtered ITO/MgF_2	[48]
Bottom c-Si cell	0.562	13.3	76.2	5.7			
Top PSC	0.95	18.8	69	12.4	20.1	MoO_x/Sputtered ITO	[49]
Bottom SHJ cell	0.64	16.9	73	7.9			
Top PSC	1.08	20.6	74.1	16.5	23.0	Cu 1 nm/Au 7 nm/BCP 40 nm	[50]
Bottom SHJ cell	0.679	12.3	77.9	6.5			
Top PSC	1.069	20.1	76.1	16.4	25.2	MoO_x/Sputtered IO:H/ITO	[51]
Bottom SHJ cell	0.693	15.98	79.5	8.8			
Top PSC	1.08	16.69	75.0	13.52	19.08	Sputtered ITO	[52]
Bottom Pb-Sn cell	0.76	9.14	80.0	5.56			
Top 1.6 eV PSC	0.97	20.3	79.0	15.8	20.3	Sputtered ITO	[53]
Bottom 1.2 eV PSC	0.74	7.9	73.0	4.5			

V_{OC} = open-circuit voltage; J_{SC} = short-circuit current; *FF* = fill factor; PCE = power conversion efficiency; PSC = perovskite solar cell; ST = semitransparent; CIGS = copper indium gallium selenide; SHJ = silicon heterojunction (amorphous/crystalline); ITO = indium tin oxide; AgNW = silver nanowire; IZO = indium zinc oxide; AZO = aluminum zinc oxide; IO:H = hydrogenated indium oxide; BCP = bathocuproine.

layer with sputtered ITO as the transparent electrode (Figure 2e,f), where FA^+ is $HC(NH_2)_2^+$. This yielded 15.1% PCE for the PSC top-cell and 7.3% PCE for the filtered SHJ bottom-cell, which gave a PSC/Si four-terminal tandem device a total PCE of 22.4%.[47]

Besides Si and CIGS solar cells, Yang et al.[52] proposed to utilize PSCs based on the narrow-bandgap $FA_{0.5}MA_{0.5}Pb_{1-x}Sn_xI_3$ HOIP as the bottom-cell for mechanical stacking with another PSC as the top-cell in a four-terminal tandem solar cell. Partially replacing the Pb^{2+} in $MAPbI_3$ by Sn^{2+} can reduce the bandgap of the HOIP, although the instability of Sn-based HOIPs remains a challenge.[34,35,54] In order to overcome the tendency of Sn^{2+} to oxidize easily, Yang et al.[52] replaced 50% of the MA^+ cations with FA^+ cations to form a 1.33 eV Pb–Sn binary HOIP, $FA_{0.5}MA_{0.5}Pb_{0.75}Sn_{0.25}I_3$, and resulting PSCs demonstrated a stabilized PCE of 14.2%. In that paper, they mentioned that partial substitution of MA^+ with FA^+ can significantly modify the electronic structure, thermal expansion coefficient, and specific heat of the HOIP, which could reduce the tendency of $Sn^{2+} \rightarrow Sn^{4+}$ oxidation, and, thus, improve its ambient stability.[52] When mechanically-stacking a semitransparent $MAPbI_3$ PSCs of

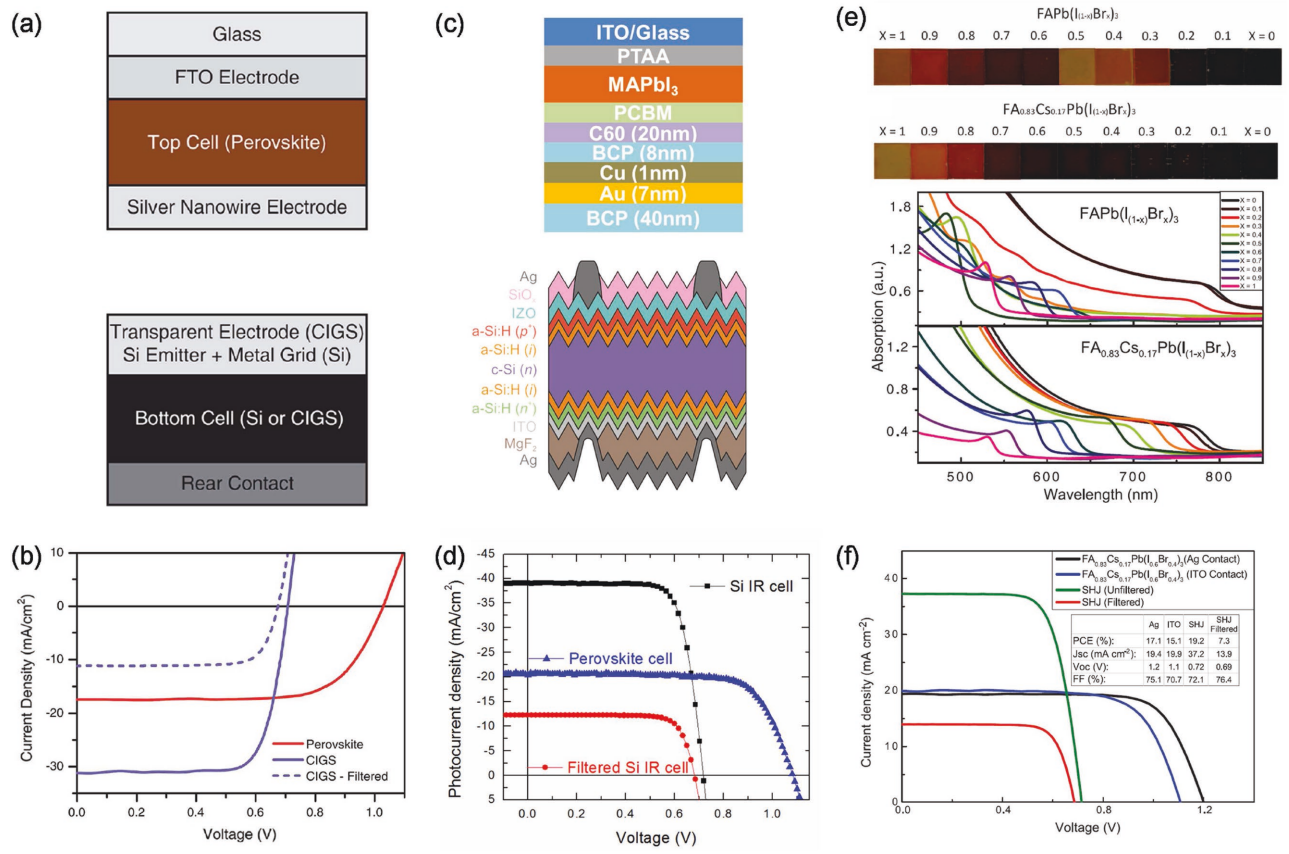

Figure 2. a) Schematic illustration and b) J-V curves of PSC/CIGS mechanically-stacked tandem solar cell based on AgNW electrode. Reproduced with permission.[39] Copyright 2015, The Royal Society of Chemistry. c) Schematic illustration and d) J-V curves of PSC/Si mechanically-stacked tandem solar cell based on ultra-thin metal electrode. Reproduced with permission.[50] Copyright 2016, Wiley-VCH. e) Photographs and absorption spectra of $FAPb(I_{1-x}Br_x)_3$ and $FA_{0.83}Cs_{0.17}Pb(I_{1-x}Br_x)_3$ HOIP thin films, and f) J-V curves of $FA_{0.83}Cs_{0.17}Pb(I_{1-x}Br_x)_3$/Si mechanically-stacked tandem solar cells. Reproduced with permission.[47] Copyright 2016, American Association for the Advancement of Science.

1.55 eV bandgap on top of $FA_{0.5}MA_{0.5}Pb_{1-x}Sn_xI_3$-based PSC, the bottom-cell still displayed 5.56% PCE, which yielded an all-PSC four-terminal tandem solar cells with 19.08% overall PCE (Table 1).[52] Similarly, Eperon et al.[53] demonstrated all-PSC four-terminal tandem device with 20.3% overall PCE based on 1.6-eV $FA_{0.83}Cs_{0.17}Pb(I_{0.83}Br_{0.17})_3$ PSC top-cell and 1.2-eV $FA_{0.75}Cs_{0.25}Sn_{0.5}Pb_{0.5}I_3$ PSC bottom-cell.

2.2. Optically-Coupled Four-Terminal Tandem Solar Cells

Another tandem concept of is based on optical coupling through spectral splitting, which uses a dichroic mirror to reflect the short-wavelength light to the wide-bandgap top-cell, and transmits the long-wavelength light to the small-bandgap bottom-cell. As a result, it can absorb the maximum portion of the incident sunlight and reduce the thermalization loss. Similar to mechanically-stacked tandem solar cell, the top-cell and bottom-cell are optimized individually without the requirement of current-matching in an optical coupling tandem solar cell. Moreover, it just requires one transparent electrode for the top-cell, which avoids the parasitic absorption loss at the transparent electrode (discussed in section 4). Due to the high cost of dichroic mirrors, it seems the application of optical coupling tandem under typical one-sun illumination is not an economically viable option, while concentrated PV systems would be the best application for optical coupling tandem devices.[55] However, the high operating temperature of the concentrated PV system creates a challenge in terms of the long-term thermal stability of the PSC.

Uzu et al.[56] demonstrated the first optically-coupled tandem solar cells using PSCs at the end of 2014. In their optical coupling system, an optical splitter with cutoff wavelength (λ) of 550 nm was positioned 45° with respect to both cells (**Figure 3**). As a result, the sunlight with wavelength shorter than 550 nm was reflected from the optical splitter to the top $MAPbI_3$-based PSC, while long wavelength light was transmitted to the bottom mono-crystalline Si heterojunction cell. The 15.3%-PCE PSC top-cell generated 7.5% PCE under the reflected light, and the 25.2%-PCE Si bottom-cell generated 20.5% PCE under the transmitted light, which gave a total PCE of 28.0% for $MAPbI_3$/Si optically-coupled tandem solar cell. They found that increasing the cutoff wavelength does not benefit the tandem performance, which was attributed to the smaller external quantum efficiency (EQE) of the PSCs top-cell compared to the Si bottom-cell at λ>550 nm in their study. Therefore, it is important to improve the EQE of the PSC top-cell for optical coupling tandem solar cells to obtain >30% PCE in the future. Uzu et al.[56] suggested that increasing V_{OC} for the PSC top-cell

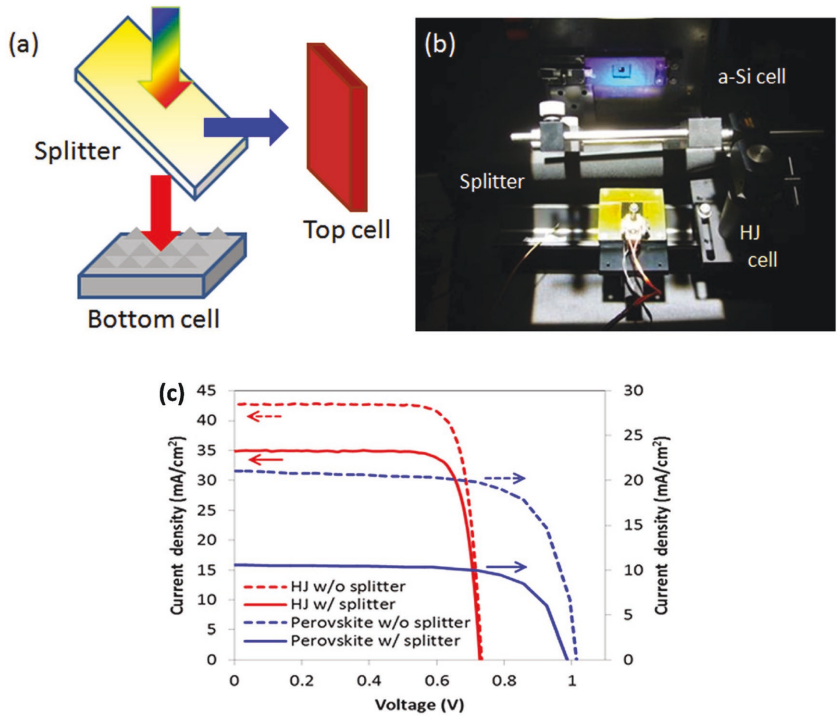

Figure 3. a) Schematic illustration of optically-coupled tandem solar cell. b) Measurement setup of an optical-splitting system. c) Comparison between J-V curves of solar cells with and without splitter for PSC/SHJ cell combination. Reproduced with permission.[56] Copyright 2015, American Institute of Physics.

without compromising the J_{SC} and EQE, can enhance the overall tandem performance. Similarly, Sheng et al.[57] used a $MAPbBr_3$-based PSC top-cell, instead of the $MAPbI_3$-based PSC top-cell, in an optically-coupled tandem solar cell. However, this only improved the 22.7%-PCE passivated-emitter rear locally-diffused (PERL) Si solar cell performance to 23.4%-PCE $MAPbBr_3$/Si optically-coupled tandem solar cell. This is because of the low EQE value (40–50%) at λ>550 nm and large $E_g/e\text{-}V_{OC}$ offset for the $MAPbBr_3$ PSC.

Optically-coupled tandem solar cells could have a broad choice of top- and bottom-cells. Besides Si cells, Kinoshita et al.[58] investigated small-bandgap dye-sensitized solar cell (DSSC) as the bottom-cell, which exhibits a broad response up to 1100 nm wavelength. Based on 18.4%-PCE pristine PSC cell and 10.2%-PCE pristine DSSC cell, they achieved 21.5% PCE for the PSC/DSSC tandem solar cell under spectral-splitting configuration. Compared to PSC/Si optically-coupled tandem, its PCE still is not very high. Even though the DX3 dye has high EQE at 400–850 nm, the V_{OC} for the DSSC cell is only 0.556 V, considering 1.18 eV bandgap for DX3, it yields ≈0.6 V voltage loss and greatly limits the tandem performance. Beside absorption of broad spectrum, for a highly efficient optically-coupled tandem solar cell, it is important to obtain high EQE value and low $E_g/e\text{-}V_{OC}$ offset for both top- and bottom-cells.

2.3. Monolithically-Integrated Tandem Solar Cells

For the monolithic tandem configuration, the PSCs top-cell is directly integrated with the bottom-cell through an intermediate layer for efficient charge transport, such that the top-cell and bottom-cell are connected in series. As a result, the photocurrent is determined by the smaller photocurrent of the two sub-cells in a monolithically-integrated tandem solar cell, and current-matching between the two sub-cells is important to avoid power loss. For the intermediate layer, it can be a tunnel junction or a recombination layer (such as SnO_2/ITO, PEDOT:PSS/ITO, P3HT/PCBM, or PFN/TiO_2/PEDOT:PSS), as shown in **Table 2**. Compared to the requirement of the three transparent electrodes in mechanically-stacked tandem solar cells, the monolithically-integrated

Table 2. Summary of intermediate layer, top-cell, bottom-cell, and photovoltaic parameters for different monolithic tandems based on PSC top-cell.

Intermediate layer	Top cell	Bottom cell	V_{OC} [V]	J_{SC} [mA cm^{-2}]	*FF* [%]	PCE [%]	Ref.
n^{++}/p^{++} tunnel junction	$MAPbI_3$	c-Si cell	1.58	11.5	75	13.7	[59]
SnO_2/ITO	$MAPbI_3$	SHJ cell	1.76	14.0	77.3	19.1	[60]
PCBM/PEIE/IZO	$MAPbI_3$	SHJ cell	1.69	15.8	79.9	21.2	[61]
PEDOT:PSS/ITO	$MAPbI_3$	CZTS	1.35	5.6	60.4	4.6	[62]
PEDOT:PSS/ITO	$MAPb(I_xBr_{1-x})_3$	CIGS	1.45	12.7	56.6	10.9	[63]
P3HT/PCBM	$MAPbBr_3$	$MAPbI_3$	1.95	8.4	66	10.8	[64]
PFN/TiO_2/PEDOT:PSS	$MAPbI_3$	PBSeDTEG8	1.52	10.05	67	10.23	[65]
C_{60}-SB/Ag/MoO_3	PCE-10:$PC_{71}BM$	$MAPbI_3$	1.63	13.1	75.1	16.0	[66]
PCBM/PEIE/IZO	$MAPbI_3$	SHJ cell	1.72	16.4	73.1	20.5	[51]
SnO_2/ITO	$FA_{0.83}Cs_{0.17}Pb(I_{0.5}Br_{0.5})_3$	$FA_{0.75}Cs_{0.25}Sn_{0.5}Pb_{0.5}I_3$	1.66	14.5	70.0	17.0	[53]

PCBM = phenyl-C_{61}-butyric-acid-methyl-ester; $PC_{71}BM$ = phenyl-C_{71}-butyric-acid-methyl-ester; PEIE = polyethylenimine; CZTS = $Cu_2ZnSn(S,Se)_4$; PFN = poly[(9,9-bis(3′-(N,N-dimethylamino)propyl)-2,7-fluorene)-alt-2,7-(9,9-dioctyfluorene)]; C_{60}-SB = tris(sulfobetaine)-substituted fulleropyrrolidine; PEDOT:PSS = poly(3,4-ethylenedioxythiophene polystyrene sulfonate; P3HT = poly(3-hexylthiophene-2,5-diyl).

tandem solar cell needs only one transparent electrode, which greatly reduces the potential parasitic absorption by the electrode, and it would also decrease the manufacturing cost.

The first prototype of monolithically-integrated PSC/Si tandem solar cell was reported by Mailoa et al.[59] in early 2015. They utilized the band-to-band n^{++}/p^{++} tunnel junction to connect the PSC top-cell and the Si-diffused homo-junction bottom-cell. The compact-TiO_2 electron-transport layer (ETL) for the PSC was deposited on top of the tunnel junction by atomic layer deposition (ALD). Subsequently, mesoporous TiO_2, $MAPbI_3$, and spiro-OMeTAD hole-transport layer (HTL) was deposited sequentially. Finally, the top transparent electrode (AgNW mesh) was mechanically transferred onto the spiro-OMeTAD surface, together with an additional 111-nm LiF anti-reflection layer. This PSC/Si monolithically-integrated tandem solar cell demonstrated a PCE of 13.7% with the limiting effect from the small J_{SC} due to parasitic absorption by spiro-OMeTAD.

For the bottom-cell in the tandem configuration, it is necessary for the Si solar cell to have better response to NIR light for large J_{SC}, and to have well-passivated surface for high V_{OC}. Among different types of Si solar cells, the a-Si:H/c-Si silicon heterojunction (SHJ) cell is the best choice for the bottom-cell to meet these two requirements.[40,60] However, the a-Si:H passivation layer is unstable at temperature >200 °C, which necessitates low-temperature fabrication processes. Similarly, CIGS solar cells also have degradation issues at temperatures >200 °C. Unfortunately, the mesoporous or compact TiO_2 in *n-i-p* PSCs structure requires high temperature annealing (300–500 °C). In order to overcome this issue, Albrecht et al.[60] deposited SnO_2 ETL at room-temperature using ALD to replace the conventional TiO_2 ETL (**Figure 4**a). Together with the ITO top layer on SHJ bottom-cell, SnO_2/ITO serves as a recombination contact between the two cells. After the deposition of MoO_3/sputtered ITO/LiF as the top transparent electrode, they fabricated an 18.1%-PCE monolithically-integrated tandem solar cell, with a high V_{OC} of 1.78 V (Figure 4b).[60] The current loss comes mainly from the parasitic absorption by the spiro-OMeTAD, and the reflection loss as the Si cell needs to be smooth which cannot trap light effectively. Another approach is to utilize organic ETL to replace the conventional TiO_2, which can be formed using low-temperature processes. Werner et al.[51,61] utilized organic PEIE/PCBM bi-layer as ETL to avoid the post-annealing for PSC top-cell, and the recombination layer between the PSC top-cell and the SHJ bottom-cell was PCBM/PEIE/IZO (Figure 4d). With spiro-OMeTAD as HTL, MoO_x as buffer layer, and sputtered IO:H/ITO stack as transparent electrode for PSC top-cell, they achieved a monolithically-integrated PSC/Si tandem solar cell with PCE as high as 20.5% for a cell area of 1.43 cm^2 (Figure 4e).[51]

Besides Si solar cell, CIGS and $Cu_2ZnSn(S,Se)_4$ (CZTS) based solar cells have also been investigated as the bottom-cell in the monolithically-integrated tandem solar cells.[62,63]

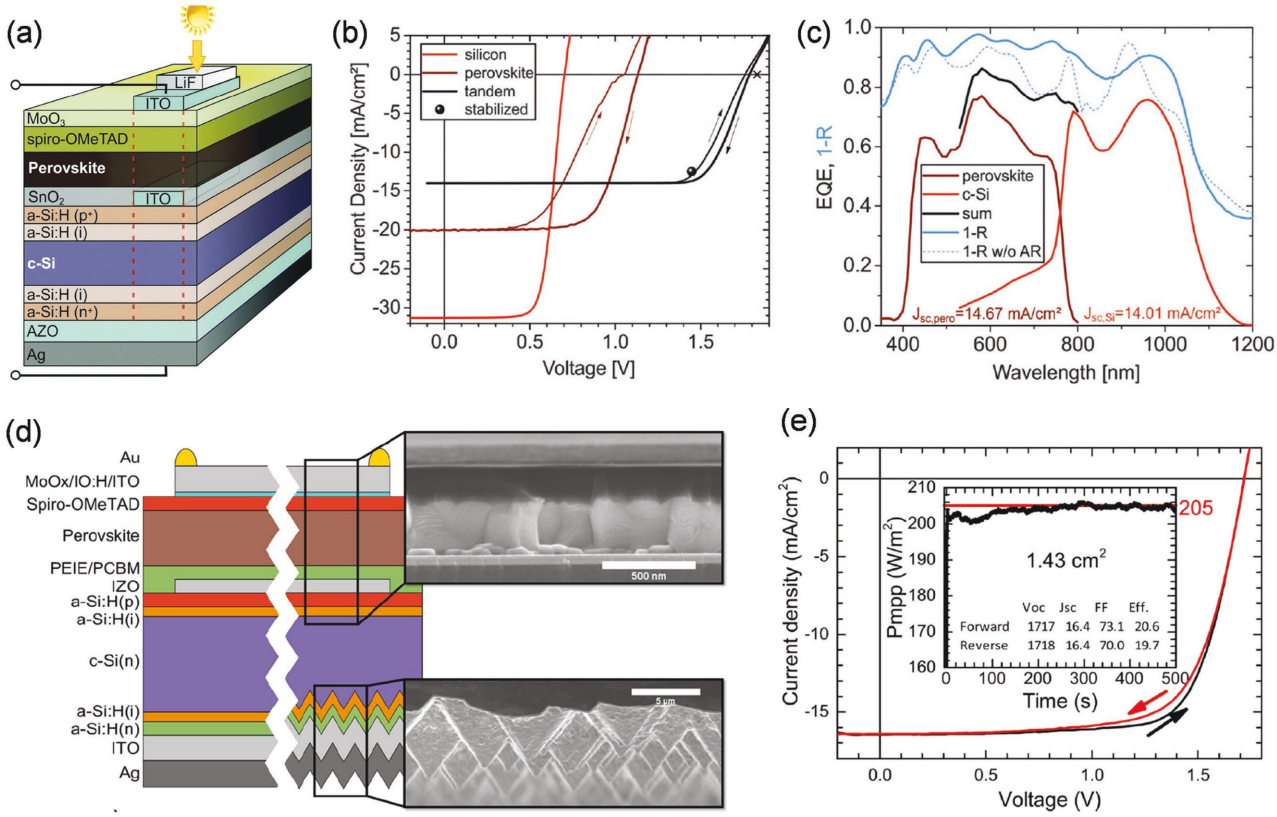

Figure 4. Monolithically-integrated PSC/Si tandem solar cell with SnO_2/ITO recombination layer: a) schematic illustration, b) J-V curves, and c) EQE and 1-reflectance. Reproduced with permission.[60] Copyright 2016, The Royal Society of Chemistry. Monolithically-integrated PSC/Si tandem solar cell with PCBM/PEIE/IZO recombination layer: d) Schematic illustration and e) J-V curves. Reproduced with permission.[51] Copyright 2016, American Chemical Society.

Teodor et al.[62,63] reported PSC/CIGS and PSC/CZTS tandem solar cells with PEDOT:PSS/ITO as the recombination connection layer. They used wide-bandgap $MAPb(I_xBr_{1-x})_3$ based PSC as the top-cell, which was fabricated by halide-exchange reaction between the MABr vapor and $MAPbI_3$ thin film.[63] Transparent electrode with 80% transmittance was fabricated by thermally evaporating 5 nm BCP/10-15 nm Ca bilayer. Even though the CIGS top-cell and the PSC bottom-cell individually displayed 11.4% PCE, the PSC/CIGS monolithic tandem solar cell delivered only 10.98% PCE in their report,[63] which was limited by the small J_{SC} due to the large optical loss in the top BCP/Ca transparent electrode. Assuming 100% transmittance from top transparent electrode, they projected that the tandem solar cell can have a PCE of 15.9%.[63]

Another interesting tandem configuration is the PSC-1/PSC-2 all-perovskite monolithically-integrated tandem solar cell.[64] Growth of second HOIP active layer on top of solvent-sensitive bottom PSCs is the main challenge for all-perovskite monolithically-integrated tandem solar cell. This is because the DMF solvent in the precursor of the second HOIP layer can dissolve the first HOIP layer in the bottom-cell. In order to overcome this challenge, Heo et al.[64] proposed to laminate the two PSCs to avoid the potential damage from the DMF solvent. As shown in **Figure 5**a, a wide-bandgap FTO/TiO_2/$MAPbBr_3$/wet P3HT (2.25 eV) front-cell was laminated with a narrow-bandgap PCBM/$MAPbI_3$/PEDOT:PSS/ITO (1.55 eV) back-cell by applying pressure and drying.[64] The relatively thick (2000 nm) P3HT (or PTAA) in the front-cell, which serves as the adhesive layer, is the key to the success of the lamination. Heo et al.[64] successfully fabricated $MAPbBr_3$/$MAPbI_3$ tandem solar cells with 1.95 V V_{OC}, 8.4 mA cm^{-2} J_{SC}, 66% *FF*, and 10.8% PCE. An exciting development in PSC-1/PSC-2 all-perovskite monolithically-integrated tandem solar cells was recently reported by Eperon et al.[53] They introduced a layer of SnO_2 coated with sputtered ITO as the recombination layer, where this compact SnO_2/ITO layer can prevent damage of the PSC bottom-cell during the direct spin-coating of the second HOIP layer. Based on the 1.8-eV $FA_{0.83}Cs_{0.17}Pb(I_{0.5}Br_{0.5})_3$ HOIP-based PSC top-cell and 1.2-eV $FA_{0.75}Cs_{0.25}Sn_{0.5}Pb_{0.5}I_3$ HOIP-based bottom-cell, Eperon et al.[53] achieved a PCE of 17.0%, with V_{OC} of 1.66 V, *FF* of 70% and J_{SC} of 14.5 mA cm^{-2} (Figure 5). Large E_g/e-V_{OC} offset (1.85 V in Heo et al.'s study and 1.34 V in Eperon et al.' study) still significantly suppresses the PV performance for the all-perovskite monolithically-integrated tandem solar cells.

PSCs have also been integrated with polymer-based solar cells in tandem structures.[65,66] The fabrication process of HOIP layer typically requires thermal treatment. If the PSCs are fabricated on top of polymer-based cells, the post-annealing could damage the polymer-based cells. Thus, it is important to find narrow-bandgap IR-polymers with excellent thermal tolerance for use as the bottom-cell to mitigate this damage. Chen et al.[65] developed a new IR-polymer, PBSeDTEG8 with E_g of 1.31 eV, to meet this requirement. They further exploited a solvent-wash method to crystallize the HOIP thin film rapidly and reduce the post-annealing temperature to 100 °C and the duration to 5 min, thus making the process compatible with polymer-based bottom-cell. This yielded a PSC/polymer monolithically-integrated tandem solar cell with 1.52 V V_{OC}, 10.05 mA cm^{-2} J_{SC}, 67% *FF*, and 10.23% PCE. Note that the sunlight enters from the bottom IR-polymer cell, which responds to both visible and IR light, and the un-absorbed visible light is harvested by the PSC top-cell. In contrast, Liu et al.[66] grew the polymer-based cell on top of the PSC to avoid the post-annealing process altogether. The absorbers in both solar cells have similar E_g of 1.55 eV in their studies. The champion tandem solar cells had a PCE of 16.0%, which was only slightly larger than that of their best standalone PSC (15.6%).

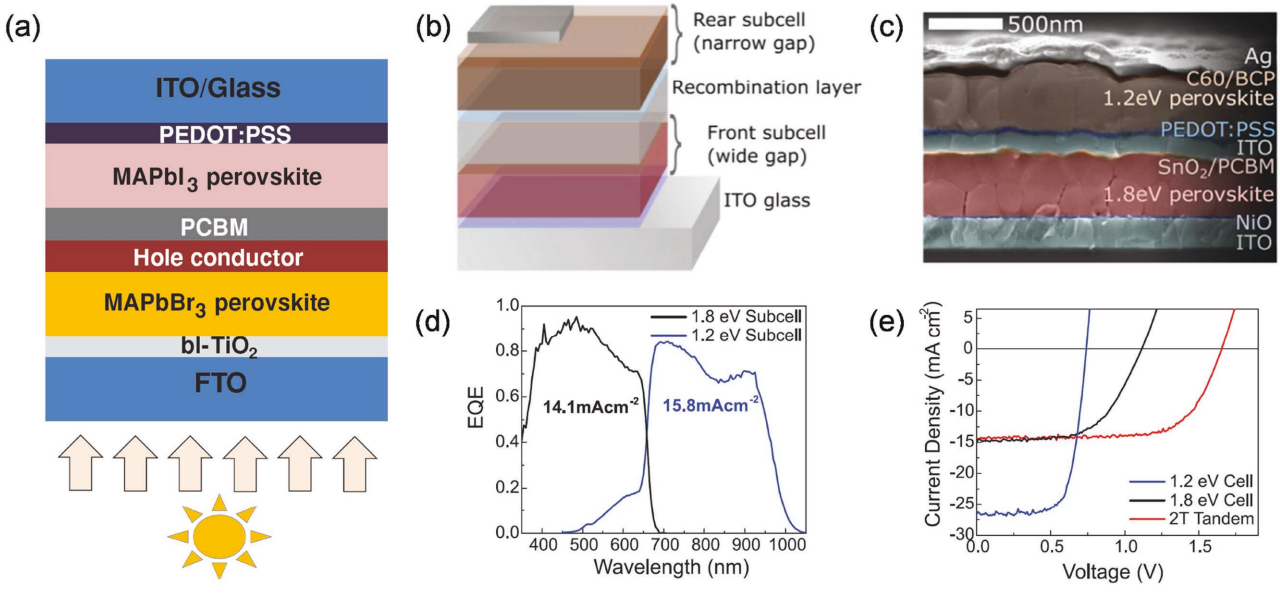

Figure 5. a) Schematic illustration of the $MAPbBr_3$/$MAPbI_3$ monolithically-integrated tandem solar cell. Reproduced with permission.[64] Copyright 2015, Wiley-VCH. b) Schematic illustration, c) SEM image, d) EQE curves, and e) J-V curves of PSC-1/PSC-2 all-perovskite monolithically-integrated tandem solar cells with 1.8 eV/1.2 eV light absorber. Reproduced with permission.[53] Copyright 2016, American Association for the Advancement of Science.

The relatively low EQE for the polymer solar cells is the limiting factor for PSC/polymer tandem solar cells.

3. Transparent Electrodes

For dual-junction tandem solar cells, it is critical to develop highly transparent and conductive electrodes for the PSC top-cells, because light comes in from the wide-bandgap PSC side. The electrode must have excellent transmittance for the incident sunlight, with a 300–1200 nm transmittance window for the electrode on top of the perovskite cell, or with 600–1200 nm transmittance window for the electrode in between the PSC top-cell and lower-bandgap Si bottom-cell. In addition to optical transmittance, the top transparent electrodes should have excellent lateral electrical conductivity for collection of photogenerated carriers, because a large sheet resistance results in significant power loss. Moreover, since HOIPs degrade when exposed to high temperatures, certain solvents, and/or highly energetic particles, the deposition process for transparent electrode needs to be 'gentle' in order to avoid potential damage to the underlying HOIP. To-date, several different types of transparent electrodes have been used, such as AgNW mesh, sputtered transparent conductive oxides (TCOs), ultra-thin metal electrodes, graphene, carbon nanotubes (CNTs), and PEDOT:PSS.

3.1. Silver Nanowire Mesh

Owing to its high electrical conductivity, good optical transmittance, convenient solution processability, and outstanding mechanical flexibility, AgNW meshes have been successfully utilized as the transparent electrode in DSSCs, organic, CIGS, and Si solar cells.[67–71] Several attempts have been made to apply AgNW electrodes to achieve semitransparent PSCs.[39,59,72–74] However, the solution-deposition process of AgNW mesh can degrade the HOIP layer; solvents or residuals from AgNW inks, such as water or ethanol, have been shown to change the HOIP from dark brown to yellowish.[73] Lee et al.[72] found that AgNW ink in isopropanol showed less damage, and the solvent deterioration time could be further reduced using the spray-coating approach with ultra-fast drying process. Also, a dense ZnO buffer layer has been introduced between the AgNW layer and the HOIP layer to prevent the reaction of the solvents with HOIP during AgNW deposition (**Figure 6**a). As a result, Guo et al.[73] reported a 8.5%-PCE semitransparent PSC with transmittance of ≈50% at 600–900 nm when illuminated from the ITO/glass side, and the sheet resistance of AgNW mesh was 20 Ω sq^{-1}. Another strategy is mechanically transferring the spray-coated AgNW mesh from a poly(ethylene tetrapthalate) (PET) film to the PSC through the application of pressure, avoiding the solvent-damage issue entirely (Figure 6c).[39,59] The transferred-AgNW transparent electrode had a sheet resistance of 14.4 Ω sq^{-1}, and it exhibited ≈90% transmission at 600–1000 nm,[39,59] which enabled a 12.7%-PCE semitransparent PSCs with illumination from the ITO/glass side, demonstrating 60–77% light transmittance at 800–1200 nm at the bottom-cell.[39]

In addition to the solvent causing HOIP degradation, another critical challenge for the application of AgNW as transparent electrodes is the relatively quick oxidation or sulfurization under ambient conditions, which severely limits the long-term stability of the electrodes and the devices.[75] Even under inert and dry atmosphere, PSCs with AgNW electrodes suffer rapid degradation as a result of the chemical reaction between the migrated or sublimed I^- with the AgNW to form insulating AgI.[73] In order to overcome this issue, Chang et al.[74] proposed to introduce a compact ZnO buffer layer between the HOIP absorber and AgNW, together with a compact Al_2O_3 encapsulation layer on top of AgNW, which improved the short-term stability of the AgNW electrodes. However, the long-term stability still needs to be addressed by finding alternative metals that are stable in contact with the HOIP. Recent demonstration of over 20-year predicted stability of Cu with HOIP opens a new window of opportunity for the application of metal NWs as transparent electrodes.[76] Future research will be needed in developing CuNW network over large areas to demonstrate their use as high-conductivity and transparent electrodes.

3.2. Sputtered Transparent Conductive Oxides

Magnetron-sputtered TCOs are widely used as transparent electrodes for solar cells, especially in Si- and CIGS-based solar cells.[77,78] However, the direct application of sputtered TCO in

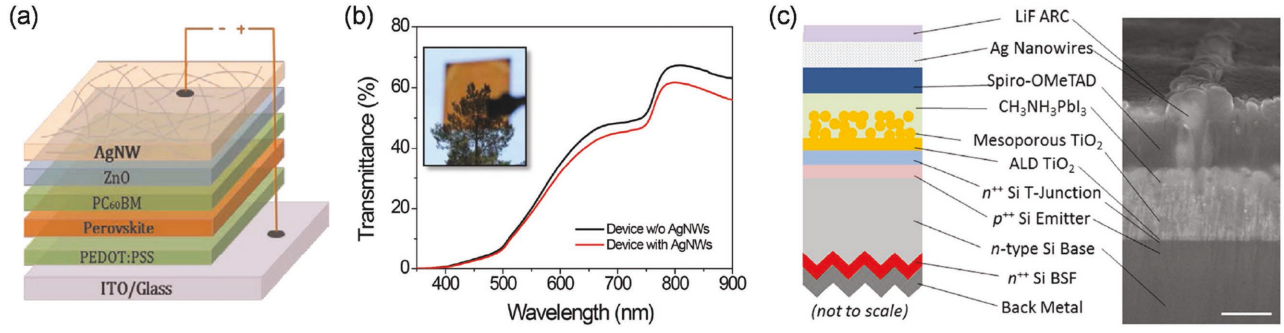

Figure 6. a) Schematic illustration and b) transmittance of semitransparent PSCs based on spin-coated AgNW with ZnO buffer layer. Reproduced with permission.[73] Copyright 2015, The Royal Society of Chemistry. c) PSC/Si monolithically-integrated tandem solar cell with mechanically-transferred AgNW as top transparent electrode. Reproduced with permission.[59] Copyright 2015, American Institute of Physics.

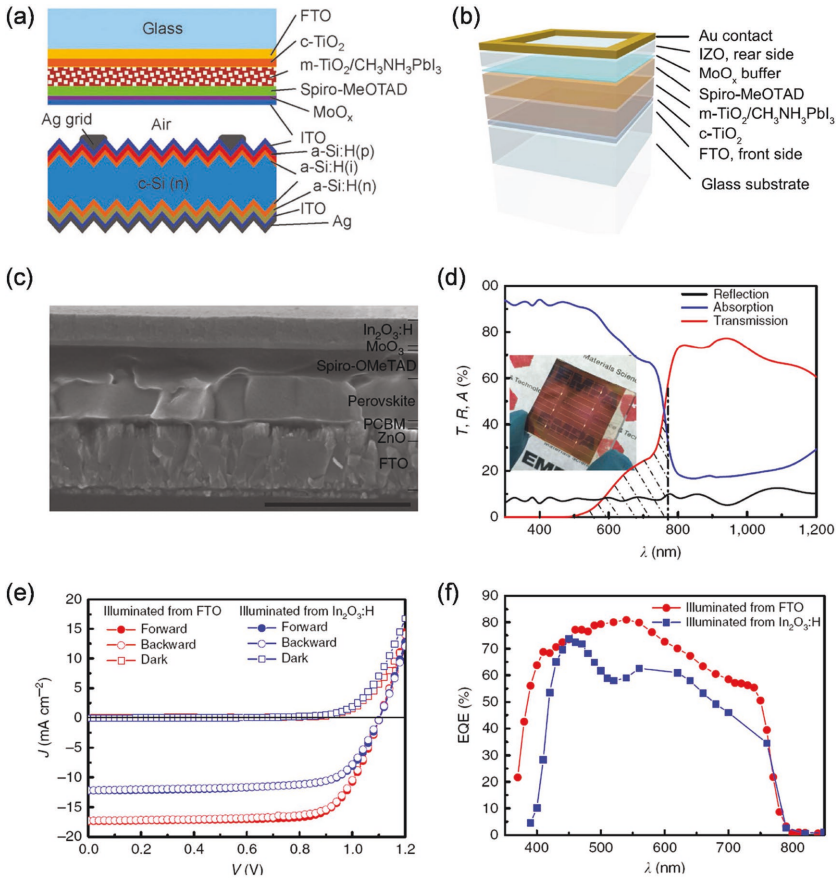

Figure 7. a) Schematic illustration of mechanically-stacked PSC/Si tandem solar cell based on sputtered ITO electrode. Reproduced with permission.[40] Copyright 2015, The Royal Society of Chemistry. b) Schematic illustration of semitransparent PSC based on sputtered IZO electrode. Reproduced with permission.[41] Copyright 2015, Elsevier. c) SEM image of semitransparent PSC with sputtered In_2O_3:H as transparent electrode. Scale bar is 1 µm. d) The transmission (T), reflection (R) and absorption (A) of the semitransparent PSC. e) J-V curve and f) EQE spectra of the semitransparent PSC. Reproduced with permission.[46] Copyright 2015, Nature Publishing Group.

perovskite solar cells faces a challenge, as the bombardment of highly energetic particles can easily damage the HOIP layer, the organic hole transport layer, and electron transport layer. Löper et al.[40] showed that direct sputtering of ITO onto the spiro-MeOTAD-coated HOIP films made the device non-rectifying, which highlights the detrimental effects of the sputtering process. This type of sputtering damage can also occur in Si heterojunction solar cells, but a subsequent high-temperature annealing treatment can almost completely heal the damage. However, such an approach is not feasible in the case of HOIPs. In this context, Löper et al.[40] deposited another hole transport layer, 30-nm inorganic molybdenum oxide (MoO_x), on top of spiro-MeOTAD as a buffer layer to shield the HOIP and the spiro-MeOTAD during sputtering, which yielded a semitransparent PSC with 6.2% PCE (**Figure 7**a). However, this semitransparent PSC had a small *FF* and large series resistance due to high-resistivity ITO layer (90 Ω sq^{-1}) without post-deposition annealing.[40]

The sputtering of amorphous IZO, AZO and hydrogenated indium oxide (In_2O_3:H) requires relatively lower power and lower temperature than that for regular ITO does, and it can significantly alleviate sputtering damage and improve the conductivity of room-temperature sputtered TCOs.[41,43,45,46] Even directly sputtering IZO onto spiro-MeOTAD can achieve a 9.7%-PCE semitransparent PSC with a sheet resistance of 35 Ω sq^{-1}.[41] With a MoO_x buffer layer (Figure 7b), the PCE was further improved to 10.3%.[41] Werner et al.[45] further boosted the PCE of semitransparent PSC with sputtered IZO electrode to 14.7% by optimizing the HOIP layer. Similar to IZO, the 'soft' sputtering process of AZO and In_2O_3:H at room temperature can also provide good transparent electrodes for semitransparent PSCs. The sheet resistance of sputtered AZO and In_2O_3:H electrode on glass was 55 Ω sq^{-1} and 25.7 Ω sq^{-1}, respectively.[43,46] Semitransparent PSC based on the sputtered In_2O_3:H transparent electrode demonstrated a PCE of 14.2%, with 72% transmittance on an average in the NIR region, and it still had 9.6% PCE under illumination from the In_2O_3:H side (Figure 7c–f). Interestingly, in contrast to Löper et al.'s result regarding high resistivity of sputtered ITO, recently several other groups have successfully fabricated more conductive ITO electrode by room-temperature sputtering, with sheet resistance of only 9.9 Ω sq^{-1}.[47,48,60]

Considering the good combination of conductivity and transmittance, and the very good long-term stability, sputtered TCOs distinguish themselves as excellent transparent electrodes for tandem devices, although the challenge of sputtering damage to the HOIP layer still remains. Moreover, the buffer layers should also have good band alignment with charge transporter layer underneath; otherwise, it will block the extraction of photo-generated charge carriers. Therefore, *p-i-n* and *n-i-p* PSCs require different types of buffer layers. To this end, inserting a buffer layer to reduce the sputtering damage and to match the work function is a popular approach in tandem solar cell development. To date, four different types of buffer layers have been introduced using magnetron sputtering: MoO_x films deposited by thermal evaporation,[40,46,61] AZO films spin-coated from nanoparticle suspensions,[48] SnO_2 films by ALD,[53] and ITO films spin-coated from nanoparticle suspension.[47] The *p*-type MoO_x can be used on top of HTL for *n-i-p* PSCs, *n*-type AZO and SnO_2 film can be used on top of ETL for *p-i-n* PSCs, and ITO film is suitable for both PSC structures.

3.3. Ultra-Thin Metal Electrode

Research on ultra-thin metal electrodes for PSCs initially targeted neutral-colored semitransparent solar cells, which still

left some amount of visible light after transmitting through the solar cell, for building integrated PVs application,[79–81] and then moved to semitransparent PSC top-cell for tandem solar cells.[42,50] Eperon et al.[79] found that the microstructured HOIP islands enabled the combination of completely absorbing and completely transparent regions to create neutral transmission. Thermal evaporation of 10-nm Au on these microstructured HOIP islands with spiro-OMeTAD layer can yield neutral-colored semitransparent PSCs (**Figure 8**a,b), which demonstrated PCE of ≈8% and transmittance of ≈30% in the visible region. If the HOIP film is very thin (180 nm), the deposition of 6-nm gold layer together with 100-nm LiF anti-reflection layer yields a semitransparent PSC with 7.3% PCE, with transmittance of 22% on an average in the visible wavelength range. However, during the Au film deposition on spiro-OMeTAD, Au atoms tend to form clusters and separated islands.[81] Au atoms are more strongly bonded to each other than to the substrate, which leads to a Volmer–Weber (island) growth mode. This not only causes large sheet resistance (250 Ω sq^{-1}), but also reduces overall transmittance due to localized surface plasmon resonance of Au islands. Gaspera et al.[81] found when a thin MoO_3 layer (1–5 nm) is deposited on top of spiro-OMeTAD as seed layer, continuous semitransparent Au film (10 nm) can be formed with a sheet resistance of 13 Ω sq^{-1}. With another layer of MoO_3 for anti-reflection, they proposed a dielectric-metal-dielectric (MoO_3–Au–MoO_3) stack as transparent electrode for semi-transparent PSCs on a 290-nm thick $MAPbI_3$ HOIP film, and obtained 13.6% PCE, with a transmittance of 7% and 40–50% in the visible and NIR regions, respectively.[81] In the case of the MoO_x–Ag–MoO_x transparent electrode, Yang et al.[42] found that Ag also forms a non-continuous film. To address this issue, they inserted 1-nm Au as a seed layer before depositing the 10-nm Ag layer to obtain a conductive electrode and a 11.5%-PCE semitransparent PSC (Figure 8d–f). For *p-i-n* PSCs, the top charge-transporting layer is ETL, but MoO_x is a hole-transporting material. Thus, MoO_x–metal–MoO_x cannot be used as top electrode for *p-i-n* PSC due to the band mismatch. Chen et al.[50] developed Cu (1 nm)/Au (7 nm)/BCP (40 nm) transparent electrode, which can be used for both *n-i-p* and *p-i-n* PSCs, and they achieved a semitransparent cell with PCE of 16.5%, and transmittance of ≈60% in the NIR region. Due to the ultra-thinness of the metal electrode, it is important to control the roughness of the HOIP film to obtain highly conductive ultra-thin metal transparent electrode.[50] Compared with sputtered TCO, ultra-thin metal electrodes deposited by thermal evaporation cause much less damage, while the transmittance is not as high as sputtered TCO due to the strong parasitic absorption.

3.4. Graphene, Carbon Nanotubes, and PEDOT:PSS

Besides the AgNW mesh, sputtered TCO, and ultra-thin metal film, several other materials have been investigated as transparent electrodes for semitransparent PSCs, such as graphene, carbon nanotubes (CNTs), and PEDOT:PSS.[44,82–85] However,

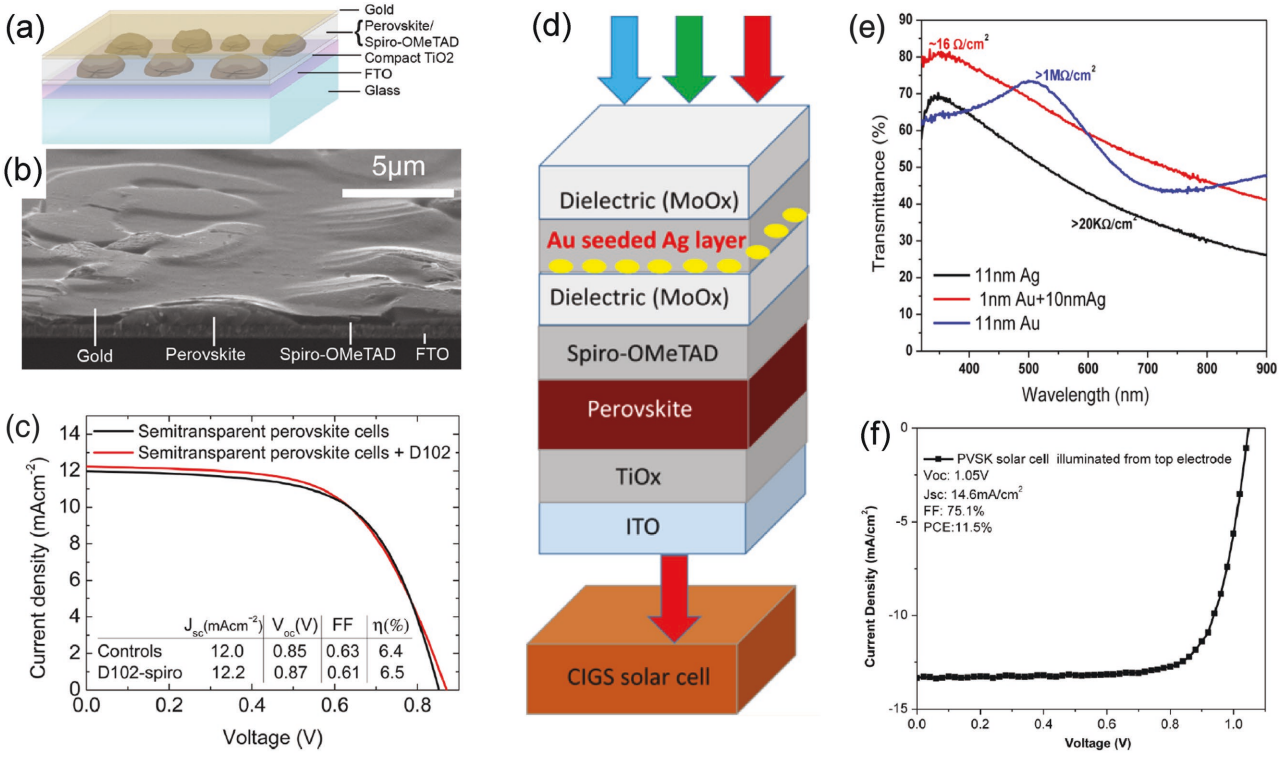

Figure 8. Neutral colored semitransparent PSC based on thin Au electrode: a) schematic illustration, b) SEM image, and c) J-V curves. Reproduced with permission.[79] Copyright 2014, American Chemical Society. d) Schematic illustration of PSC/CIGS mechanically-stacked tandem solar cell with MoO_x–Au/Ag–MoO_x as top electrode. e) Transparence and conductivity of pristine Ag, Au-seeded Ag, and pristine Au film. f) J-V curve of the optimized semitransparent PSC. Reproduced with permission.[42] Copyright 2015, American Chemical Society.

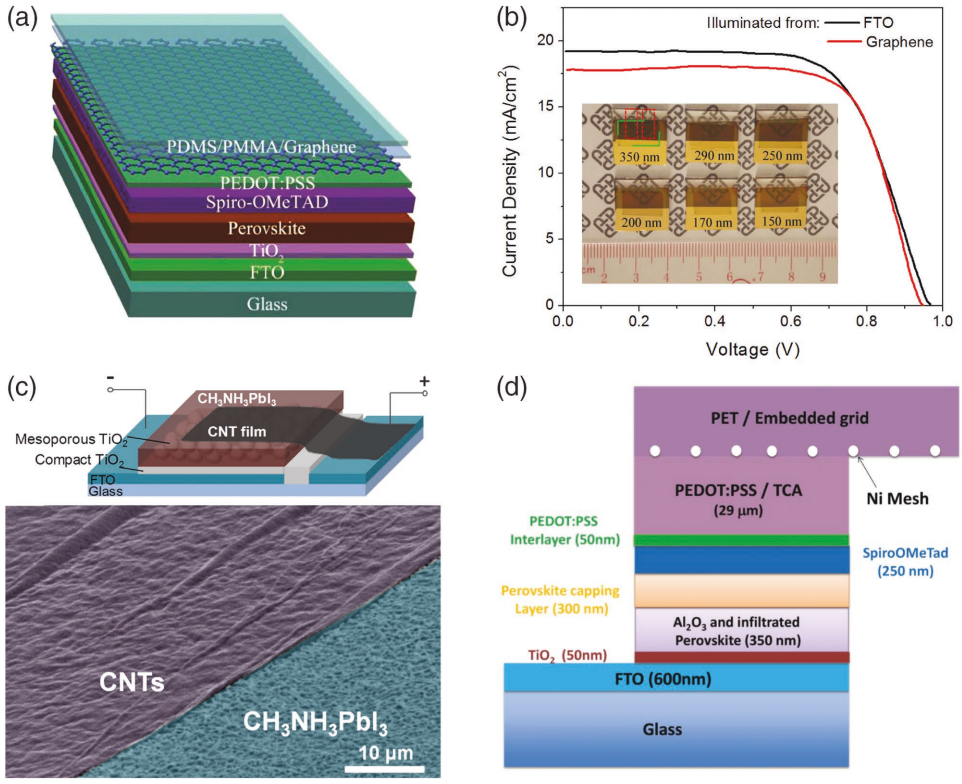

Figure 9. a) Schematic illustration of semitransparent PSC with graphene as transparent electrode. b) J-V curves for semitransparent PSC with graphene under illumination from ITO and glass sides. Inset: photos of semitransparent PSCs based on graphene electrode with different thicknesses of the HOIP layers. Reproduced with permission.[82] Copyright 2015, Wiley-VCH. c) Schematic illustration and SEM image of $MAPbI_3$-based PSC with CNT film electrode. Reproduced with permission.[83] Copyright 2014, American Chemical Society. d) Schematic illustration of semitransparent PSC with PEDOT:PSS on Ni-mesh as electrode. Reproduced with permission.[85] Copyright 2014, Wiley-VCH.

the challenge for those transparent electrodes is how to obtain the excellent conductivity and excellent transmittance at the same time.

Owing to its excellent optical transparency, high electrical conductivity, and excellent mechanical and chemical robustness, graphene shows great promise as transparent electrode for PSCs. You et al.[82] transferred chemical-vapor-deposition (CVD) grown graphene onto flexible poly(methyl methacrylate) (PMMA) and laminated it onto spiro-OMeTAD/HOIP at 60 °C under pressure to fabricate the top electrode (**Figure 9**a). Before lamination, 20-nm PEDOT:PSS was spin-coated onto graphene to reduce its sheet resistance to 140 Ω sq^{-1}, while maintaining >90% transmittance in the visible region. Subsequently, D-sorbitol was introduced on PEDOT:PSS as an 'electric glue' between PEDOT:PSS and spiro-OMeTAD for better lamination. As a result, the semitransparent PSCs with graphene electrode showed excellent bifacial PV performance (Figure 9b), with a PCE of 12.02% and 11.65% under illumination from glass side and graphene side, respectively.[82] Lang et al.[44] found that direct transfer of graphene onto PSC without the PEDOT:PSS layer can still result in decent PV performance.

CNT films as transparent electrode for semi-transparent PSCs have been reported by Li et al.[83] (Figure 9c), where they transferred freestanding CNT films on to HOIP and spiro-OMeTAD/HOIP, and obtained semi-transparent PSCs with PCEs of 6.87% and 9.90%, respectively. However, the CNT films have high sheet resistance (2–5 K Ω sq^{-1}) and low transmittance (average visible transmittance ≈60%), which leads to low *FF* (<55%) and low J_{SC} for the resulting semitransparent PSCs.[83]

Learning from the successful implementation of high-conductivity PEDOT:PSS electrode in organic PVs (OPVs), Jiang et al.[84] transferred a 120-nm PEDOT:PSS film (with polydimethylsiloxane (PDMS) as the transfer substrate) onto spiro-OMeTAD-coated HOIP as top electrode, and fabricated semitransparent PSCs with average PCE of 9.05%. Bryant et al.[85] developed a transparent-conductive adhesive by coating 29-μm PEDOT:PSS onto a Ni-mesh (with 300 μm spacing) embedded PET film (Figure 9d), which has a sheet resistance as low as 1.2 Ω sq^{-1} and a transmittance as high as 80–90% in the visible and the NIR regions. They laminated this film onto spiro-OMeTAD/HOIP as transparent electrode and obtained 13.3% PCE in the resulting semi-transparent PSCs.[85]

4. Wide-Bandgap HOIPs

Simulations have shown that a high-PCE PSC top-cell with bandgap around 1.70–1.85 eV can boost the PCE of commercial PVs to 30% using the tandem structure.[3,6,7] The bandgap of the most widely studied $MAPbI_3$ HOIP is only 1.55 eV, therefore, it is important to develop high-PCE PSCs

Table 3. Summary of the performance of wide-bandgap PSCs.

Perovskite materials	E_g [eV]	V_{OC} [V]	J_{SC} [mA cm^{-2}]	*FF* [%]	PCE [%]	Ref.
$MAPb(I_{0.71}Br_{0.29})_3$	1.71	0.96	14.2	68.9	9.37	[86]
$MAPbI_{2.4}Br_{0.6}$	1.72	1.02	17.5	73.7	13.1	[87]
$MAPbI_2Br$	1.8	1.09	14.81	62.0	10.03	[88]
$MAPb(I_{1-x}Br_x)_3$	1.72	1.01	16.1	70.2	11.4	[63]
$MAPbI_{2.5}Br_{0.5}$	1.69	1.16	18.3	78.2	16.6	[89]
$MAPbI_{2.2}Br_{0.8}$	1.75	1.21	15.8	77.9	14.9	[89]
$MAPbI_2Br$	1.77	1.08	15.3	64.7	10.7	[90]
$FA_{0.83}Cs_{0.17}Pb(I_{0.6}Br_{0.4})_3$	1.74	1.2	19.4	75.1	17.1	[47]
$CsPbI_2Br$	1.9	1.06	10.9	58.9	6.8	[92]
$MAPbI_{2.1}Br_{0.9}$	1.75	1.01	18.19	69.0	12.67	[97]
$Cs_3Bi_2I_9$	2.2	0.85	2.15	60.0	1.09	[93]
$CsPbI_3$	1.73	1.23	13.47	65.0	10.77	[96]

with a bandgap around 1.70–1.85 eV for tandem application. To date, as shown in **Table 3**, a broad range of wide-bandgap HOIPs has been explored, including $MAPb(I_{1-x}Br_x)_3$,[63,86–90] $FAPb(I_{1-x}Br_x)_3$,[91] $FA_{0.83}Cs_{0.17}Pb(I_{1-x}Br_x)_3$,[47] $CsPb(I_{1-x}Br_x)_3$,[92] $Cs_3Bi_2I_9$,[93] $Cs_2AgBiBr_6$,[94] $CsPbI_3$,[95,96] etc. There has been a unique challenge in stabilizing wide-bandgap HOIPs under illumination, although these materials can easily deposited and are stable in the dark. Therefore, tremendous efforts have been devoted to fabricating photo- and thermally-stable wide-bandgap HOIPs by optimizing their composition and grain morphology, although good thermal-stability does not always guarantee good photo-stability.

4.1. Fabrication of Wide-Bandgap HOIPs

In order to increase the bandgap of HOIPs, the principal strategy is to partially substitute I^- by Br^- to form mixed-halide HOIPs. Noh et al.[86] were the first to show that the bandgap of $MAPb(I_{1-x}Br_x)_3$ HOIP light absorbers increases monotonically, but non-linearly, with increasing Br content in the precursors, with tunable bandgap from 1.55 eV to 2.3 eV. Simple spin-coating of a $MAPb(I_{1-x}Br_x)_3$ precursor from DMF solvent is assumed to result in the corresponding $MAPb(I_{1-x}Br_x)_3$ compound (**Figure 10**a–c), although there is no evidence that the I/Br ratios in the films equal that

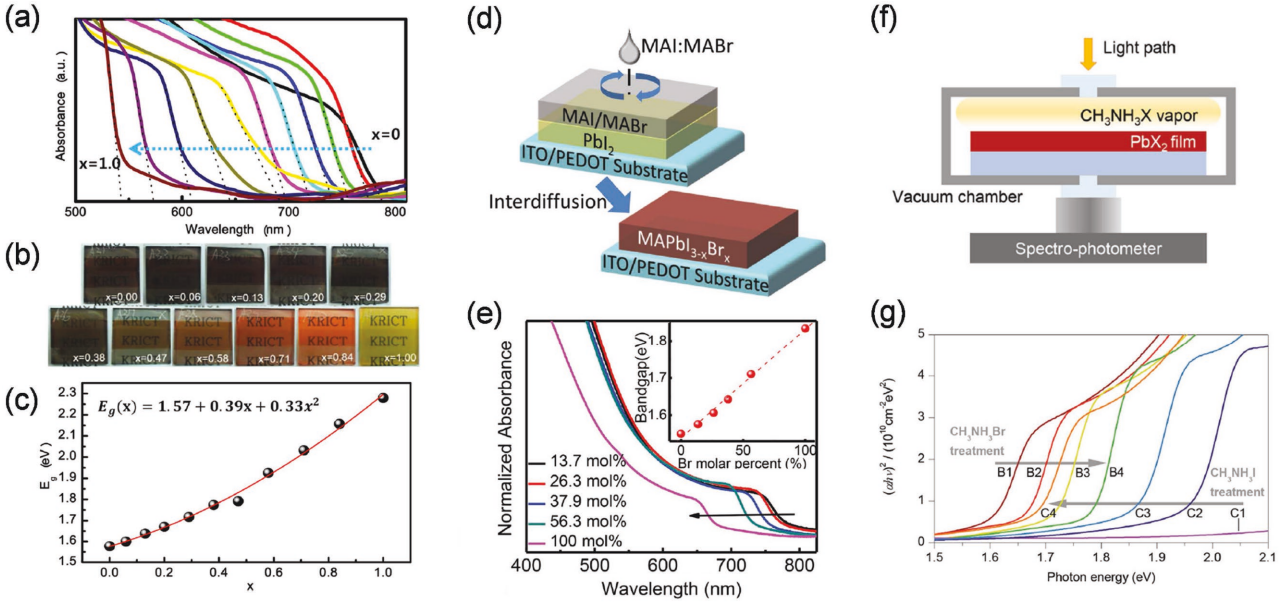

Figure 10. Mixed-halide $MAPbI_{3-x}Br_x$ films with different Br content: a) absorption spectra, b) photographs, and c) bandgap. Red curve in (c) is quadratic fitting of the bandgap as a function of Br composition. Reproduced with permission.[86] Copyright 2013, American Chemical Society. d) Schematic illustration of interdiffusion-solution method to prepare mixed-halide $MAPbI_{3-x}Br_x$ films. e) Absorption spectrum of mixed-halide $MAPbI_{3-x}Br_x$ film fabricated by the interdiffusion-solution method. Reproduced with permission.[87] Copyright 2015, Wiley-VCH. f) Schematic illustration of halide-exchange method to grow $MAPbI_{3-x}Br_x$ film with in situ band gap tuning apparatus. g) Absorption spectra of $MAPbI_{3-x}Br_x$ films prepared by halide exchange under MAI and MABr vapor. Reproduced with permission.[63] Copyright 2015, Wiley-VCH.

in the respective solutions. At a Br content of 29% among the halide ions, the resulting $MAPb(I_{1-x}Br_x)_3$ HOIP has an optical bandgap of 1.71 eV, and PSCs based on this wide-bandgap HOIP showed a J_{SC} of 14.2 mA cm^{-2}, V_{OC} of 0.96 V, and PCE of ≈10%.[86] However, the HOIP film quality in this early study was not the best, which caused charge recombination issues and limited the photocurrent density. In an effort to improve the quality of the HOIP grains, the solid-state interdiffusion method combined with a solvent annealing process has been developed by Cheng et al.[87] for the deposition of wide-bandgap $MAPb(I_{1-x}Br_x)_3$. They first spin-coated a PbI_2 thin film onto PEDOT:PSS, and then MAI/MABr blended precursor solution with different blend ratios were spin-coated onto the PbI_2 layers. Finally, the mixed-halide $MAPb(I_{1-x}Br_x)_3$ was solvent-annealed with DMF atmosphere (Figure 10d). Solvent-annealing facilitated the growth of large grains,[30] and the composition of $MAPb(I_{1-x}Br_x)_3$ perovskite was tuned by changing the MAI/MABr ratio in the blended precursor solution to obtain a bandgap that is optimized for a most efficient PSC/Si tandem solar cell. MAI/MABr blended solution (40 mg mL^{-1}) with 56.3 mol% MABr yielded $MAPbI_{2.4}Br_{0.6}$ mixed-halide HOIP with a bandgap of 1.72 eV, which had a PCE of 13.1% with PCBM as the electron transport layer.

A third approach to make mixed-halide wide-bandgap HOIP films was reported by Zhao et al.[88] is based on a thermal-decomposition method. A compact layer of $MAPbI_2Br$ film with bandgap of 1.8 eV was prepared by thermal decomposition from a spin-coated film using precursor containing PbI_2, MABr, and MACl. MACl served as the 'glue' to control the initial film formation, and the Cl evaporated during the post-annealing treatment. They fixed the ratio of PbI_2 and MABr at 1:1 to obtain a bandgap of 1.8 eV for the final HOIP films. The PSC fabricated from these compact mixed-halide HOIP films with claimed composition of $MAPbI_2Br$ achieved an overall PCE of ≈10%. Finally, Teodor et al.[63] reported a halide-exchange approach to fabricate mixed-halide $MAPb(I_{1-x}Br_x)_3$ HOIPs by exchanging I^- in $MAPbI_3$ film with Br^- from MABr vapor, resulting in an increase in the bandgap (Figure 10f). They designed a reactor where the temperature and the pressure are controlled precisely, and the optical properties of the HOIP layer are monitored in situ. The advantage of this approach is that the composition, and hence the bandgap, of the HOIP layer could be controlled through MABr-vapor treatment, while monitoring it real-time. There may be compositional inhomogeneities in the HOIP films formed by these methods in the initial stages, but the quick ion-migration should make the films homogenous after moderate thermal annealing and/or light illumination. The PSCs based on these wide-bandgap HOIPs (1.65–1.75 eV) achieved PCE around 10%–12%, and the tandem solar cells showed a PCE of 15.9%.

There have been no studies comparing the HOIP films formed by these different approaches. The different device structures applied in the different studies make it difficult to evaluate what the best approach is to make high-quality wide-bandgap HOIP films. We can suggest a simple evaluation of grain size and photoluminescence (PL) life time as a practical method to evaluate the film quality.

4.2. Light Stability of Wide Bandgap PSCs

Although wide-bandgap HOIPs can be achieved by tuning the halide composition, the segregation and phase separation of HOIP active layer within some mixed-halide wide-bandgap HOIPs with large Br content under light illumination is a new phenomenon that is detrimental to the PV performance and an obstacle in the path of application of PSCs in high-efficiency tandem solar cells. For $MAPb(I_{1-x}Br_x)_3$ HOIPs with $0.2 < x < 1$, Hoke et al.[98] first reported the formation of a new red-shifted peak at 1.68 eV upon light-soaking, which is accompanied by the growth of sub-bandgap absorption states and a splitting of XRD peaks. They speculated that light-induced halide segregation resulted in the formation of I-rich domains and Br-rich domains in the $MAPb(I_{1-x}Br_x)_3$ thin films, which could cause photo-instability in mixed-halide wide-bandgap HOIPs.[98] The invariable new PL peak at 1.68 eV from low-bandgap phase indicates that it is not feasible to attain phase-stable $MAPb(I_{1-x}Br_x)_3$ with bandgap larger than 1.68 eV. Thus, there is an urgent need to develop a facile route for stabilizing wide-bandgap HOIPs under light.

The first proposed strategy is to grow HOIP films with larger grain size to improve the photo-stability of wideband-gap PSCs. Hu et al.[89] applied a hydrophobic HTL PTAA for wide mixed-halide HOIP grain growth, which was first demonstrated by Cheng et al. to facilitate the growth of large grain films.[99] In striking contrast, by enlarging the grain size of the mixed-halide perovskite films with hydrophobic HTL PTAA, they found that the $MAPb(I_{1-x}Br_x)_3$ with bandgap of 1.70 eV to 1.75 eV were stable under 1-sun continuous illumination for 30 min without notable degradation, as evidenced by the lack of splitting of the XRD peaks.[100] The more stable HOIP also enhanced the PCE to 16.6% for the mixed-halide HOIP with a bandgap of 1.70 eV, which is among the highest for a wide-bandgap PSC. The enhancement of photo-stability by this method can be explained based on the suppression of ion-migration in larger grain size. Shao et al.[101] revealed that ion-migration occurs predominantly through the grain boundaries, as ion-migration through the grain interior is much slower. Considering that the phase separation of mixed-halide $MAPb(I_{1-x}Br_x)_3$ is caused by ion-migration, large-grain HOIP films with fewer grain boundaries should be more stable because of the reduced ion-migration pathways.

Another approach for stabilizing wide-bandgap PSCs is to partially-substitute organic MA^+ and/or FA^+ by inorganic cesium (Cs^+) in the A-site of the ABX_3 perovskite structure, which can reduce the Goldschmidt tolerance factor and improve the stability of the HOIP film. McMeekin et al.[47] made highly crystalline and compositionally photo-stable HOIP thin films, $FA_{0.83}Cs_{0.17}Pb(I_{0.6}Br_{0.4})_3$, with an optical band gap of ≈1.74 eV, and the corresponding PSCs reached V_{OC} of 1.2 V, and PCEs of >17% on small-area PSCs and 14.7% on large-area PSCs. Mixed-cation $FA_{0.83}Cs_{0.17}Pb(I_{1-x}Br_x)_3$ HOIPs as a function of $0 < x < 1$ show a continuous series of dark films and sharp optical band-edges throughout this entire compositional range. No significant red-shift in PL emission for $FA_{0.83}Cs_{0.17}Pb(I_{0.6}Br_{0.4})_3$ HOIP film was observed after 1-hour light illumination. The optical band gap and the crystal structure of the $FA_{0.83}Cs_{0.17}Pb(I_{0.6}Br_{0.4})_3$ HOIP were also stable

under thermal treatment at 130 °C.[47] Moreover, Beal et al.[92] found that replacing MA^+ by Cs^+ can also improve photo- and thermal-stability of wide-bandgap $CsPb(Br_xI_{1-x})_3$ inorganic perovskites, which is also attributed to the reduced Goldschmidt tolerance factor to a more stable value. By substituting I^- within the $CsPbI_3$ lattice with 33% Br yielded a bandgap of 1.9 eV and a PSC with a stabilized PCE of 6.5%.

4.3. New Phase Stable Wide-Bandgap Perovskites

PSCs based on lead-free wide-bandgap metal-halide perovskites, such as $Cs_3Bi_2I_9$, $MA_3Bi_2I_9$, and $MA_3Bi_2I_9Cl_x$, have also been investigated with stable PV performance. PSCs with $Cs_3Bi_2I_9$ absorber showed the highest performance among those devices, and a PCE over 1% was reported.[93] The light absorption spectra of $Cs_3Bi_2I_9$ showed only very minor change after one month storage, which indicates that this perovskite is very stable. Even though $Cs_3Bi_2I_9$ had a bandgap of 2.2 eV, the V_{OC} for $Cs_3Bi_2I_9$ solar cell was only 0.85 V, which demonstrates a V_{OC} loss of 1.35 V. Moreover, the J_{SC} was only 2.15 mA cm^{-2} and EQE value was below 40% in the visible light region. Park et al.[93] attributed this low PV performance to the extra states within the bandgap in $Cs_3Bi_2I_9$ film, un-optimized charge transport layers, and poor film morphology. Bismuth-halide double perovskite $Cs_2AgBiBr_6$, reported by Slavney et al.,[94] has an indirect bandgap of 1.95 eV, which is suited for tandem solar cells. $Cs_2AgBiBr_6$ shows a long PL lifetime of 660 ns, and significantly better heat- and moisture-stability compared to $MAPbI_3$. Even though its PV performance has not been investigated as yet, the extremely promising optical and physical properties of $Cs_2AgBiBr_6$ have motivated further exploration of both inorganic and hybrid organic-inorganic double-perovskites for photovoltaics and other optoelectronic applications. To date, the low PCE of PSCs based on lead-free wide-bandgap metal-halide perovskites has limited their application in tandem solar cells.[93,94]

The all-inorganic $CsPbI_3$ perovskite with bandgap ≈1.73 eV makes it a potential candidate for the wide-bandgap PSCs. However, $CsPbI_3$ is unstable in the desirable 'black' α-phase (E_g = 1.73 eV) under ambient conditions, and rapidly degrades to the undesirable orthorhombic 'yellow' phase with an E_g of 2.82 eV, because the yellow phase is thermodynamically stable in bulk crystals below 320 °C. It is important to improve the stability of the α-$CsPbI_3$ at room temperature under ambient conditions. Eperon et al.[95] reported that the $CsPbI_3$ precursor with HI additive could reduce the formation temperature of α-$CsPbI_3$ and enhance its phase stability. They found that films processed with HI could create lattice strain and allow lower-temperature phase transition, and it could yield a small grain size (≈100 nm) of $CsPbI_3$, which is likely responsible for stabilizing the black phase. Swarnkar et al.[96] further improved the stability of the black $CsPbI_3$ by developing α-$CsPbI_3$ quantum dots, which introduced large surface energy to retain that phase. They synthesized α-$CsPbI_3$ quantum dots with 9-nm size, and found that prolonged annealing at temperature >200 °C coarsens the $CsPbI_3$ particles, inducing the black-to-yellow phase transition. PSCs based on spin-coated film with α-$CsPbI_3$ quantum dots achieved a PCE of 10.77%, V_{OC} of 1.23 V, J_{SC} of 13.47 mA cm^{-2}, and *FF* of 65.0%. Swarnkar et al.[96] suggested that a better understanding of the electronic coupling to maximize the long-range charge transport in quantum dots perovskite films would be important to improve its performance.

5. Power Loss in PSC-Based Tandem Solar Cells – Path Towards Higher Efficiency

Understanding the loss of power in tandem devices is very important for improving the performance of PSC-based tandem solar cells. Compared to single-junction solar cells, there are additional power-loss channels in the tandem solar cells, including optical (reflection loss and parasitic absorption) and electrical (resistive) losses. **Figure 11** demonstrates optical loss in a monolithic $MAPbI_3$/Si tandem solar cell, where the white color shows the reflection loss at different wavelengths, and the other colors illustrate the absorption in each layer.[102] When the absorbed photons at some layers in a tandem solar cell do not contribute to the photocurrent, they cause parasitic absorption loss. For monolithically-integrated tandem solar cells, there is another possible power-loss channel — current mismatching. Therefore, it is essential to minimize the power loss to boost the photovoltaic performance for tandem solar cells. These power-loss channels are generic to any type of tandem solar cells, but here we focus on those that are specific to PSC-based tandem solar cells.

5.1. Reflection Loss

Due to the refractive index (n) mismatch of the multiple layers, the reflection loss leads to a significant amount of power loss in tandem solar cells, especially for long-wavelength light, as demonstrated by white color in Figure 11. Two main reflection losses occur at the front transparent electrode and the smooth Si bottom-cell surfaces.

The large refractive index differences between air (n = 1), glass (n = 1.52), and transparent electrode create remarkable reflection loss at the front electrode. Part of the light is reflected away from the higher refractive index layers without conversion into photocurrent. Figure 11 shows that the total reflection leads to photocurrent loss of 7.77 mA cm^{-2} for a monolithic $MAPbI_3$/Si tandem solar cells. In order to reduce the optical reflection loss, one approach is to deposit quarter-wavelength antireflection coatings (e.g., LiF, MgF_2).[49,60] For example, as simulated by Duong et al.,[49] with 100-nm MgF_2 antireflection coating, the reflectance loss can be suppressed to 2.33 mA cm^{-2} for PSCs. Similarly, for the monolithically-integrated tandem solar cells with sputtered-TCO as top electrode, LiF and MgF_2 antireflection coatings have also been used to minimize reflection loss.[60]

Another strategy for minimizing reflection loss is light trapping by textured front surface. To date, the PSCs are typically fabricated on smooth Si or CIGS bottom-cell in monolithically-integrated tandem configuration, otherwise the very large roughness of the texture in Si solar cells would cause very easy shunting of the PSCs. Without the textured Si light-trapping surface, the small-refractive-index HOIP layer (n ≈ 2) on top

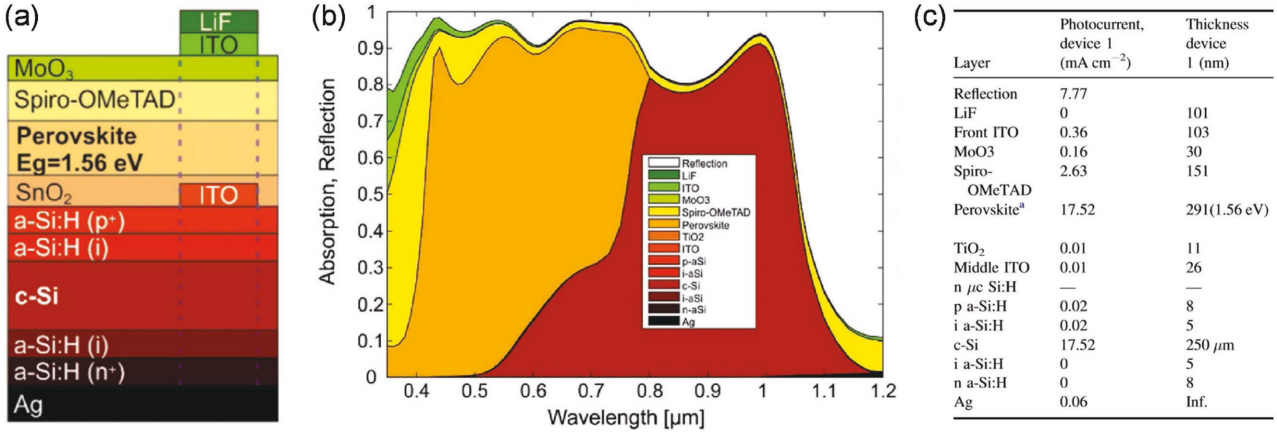

(c)

Layer	Photocurrent, device 1 (mA cm^{-2})	Thickness device 1 (nm)
Reflection	7.77	
LiF	0	101
Front ITO	0.36	103
MoO3	0.16	30
Spiro-OMeTAD	2.63	151
Perovskite[a]	17.52	291(1.56 eV)
TiO_2	0.01	11
Middle ITO	0.01	26
n μc Si:H	—	—
p a-Si:H	0.02	8
i a-Si:H	0.02	5
c-Si	17.52	250 μm
i a-Si:H	0	5
n a-Si:H	0	8
Ag	0.06	Inf.

Figure 11. a) A simulated monolithically-integrated PSC/Si tandem device solar cells structure, b) breakdown of absorption and reflection versus wavelength for a monolithically-integrated PSC/Si tandem solar cell, and c) simulated photocurrent and optimized thicknesses of each layer. Reproduced with permission.[102] Copyright 2016, IOP Publishing.

of smooth, high-refractive-index Si wafer ($n \approx 4$) would cause several mA cm^{-2} current loss, especially for long-wavelength photons which require large absorption depth.[60,102] It has been proposed that direct fabrication of PSC top-cell on a textured silicon bottom-cell can reduce the reflection loss to as low as 0.52 mA cm^{-2}.[103,104] However, the growth of high-PCE PSCs on textured Si bottom-cell is still a big challenge. Therefore, the reduction of refractive-index mismatch inside the tandem solar cells, and possible light-trapping, are important for reducing reflection loss at the front surface, and at the interface between the top-cell and the bottom-cell. A similar light-trapping idea is to attach an inverted micro-pyramidal structured polydimethylsiloxane (PDMS) in front of the glass surface as an antireflection layer,[105] improving the PCE of single-junction PSCs from 17.2% to 17.7%, which can also be used in tandem solar cells.

5.2. Parasitic Absorption

The absorption of photons in the HOIP layer and the Si layer for the PSC/Si tandem solar cell generates photocurrent, however, the absorbed photons at other layers (antireflection layer, transparent electrode, ETL, HTL, recombination layer, bottom electrode, etc.) do not contribute to the photocurrent, causing parasitic absorption loss. The difference between EQE curve and absorbance spectrum can be used to experimentally characterize the parasitic absorption loss.[40] On the other hand, the optical absorption and corresponding parasitic absorption loss in each layer can also be simulated from the optical index data.[38,102,106] The two primary parasitic absorption losses occur at the transparent electrode and at the spiro-OMeTAD layer in some *n-i-p* PSCs.

The optical absorption in the transparent electrode is an inevitable channel for photocurrent loss in both the top-cell and the bottom-cell. The parasitic loss in transparent electrode is induced by free-carrier absorption. Therefore, a lower carrier-concentration in the transparent electrode will mitigate parasitic loss, but this would increase the sheet resistance and corresponding electrical loss. There is always a trade-off between parasitic loss and electrical loss for any transparent electrode. A photocurrent loss of 0.4–1.25 mA cm^{-2} from sputtered ITO electrode has been reported in PSC/Si tandem solar cells.[38,49,102] Thinner ITO is proposed to reduce this parasitic absorption.[102] Another strategy is to replace the ITO electrode by other electrode with lower carrier-concentration but large carrier-mobility, such as IZO, to reduce the parasitic absorption. Compared to sputtered TCO, the thin metal electrodes demonstrate very large parasitic loss due to strong plasmonic absorption.[42,50] Considering that mechanically-stacked tandem solar cells require three transparent electrodes, the parasitic loss at the transparent electrode is a significant challenge in terms of reaching high PCE.

As demonstrated in Figure 11, when a spiro-OMeTAD is used as HTL for *n-i-p* PSCs top-cell, it can create a parasitic absorption loss as large as 2.63 mA cm^{-2}.[102] In addition to the parasitic absorption in the visible region, Albrecht et al.[102] reported that the spiro-OMeTAD layer also has 0.7 mA cm^{-2} parasitic absorption in the NIR region, as shown in Figure 11b. This means it will still cause additional current loss even when the spiro-OMeTAD HTL is placed at the rear electrode side in both four-terminal and two-terminal tandem solar cells. Therefore, it is important to reduce the spiro-OMeTAD layer thickness or replace it with another HTL material with less parasitic absorption. To this end, an effective solution is to utilize inverted *p-i-n* structure PSCs with very thin HTL with negligible parasitic absorption, such as PTAA, PEDOT:PSS, and NiO.

5.3. Electrical Power Loss

As deduced by Meier et al.,[107] the electrical power loss caused by sheet resistance is proportional to the product of the current density at the maximum power point (J_{MPP}) and the sheet resistance. Therefore, the sheet resistances of transparent electrode, ETL, and HTL could play an important role in determining the total PCE. As discussed in the previous section, reducing the thickness or the carrier concentration of transparent electrodes can suppress the parasitic absorption. However, this will usually increase the sheet resistance and lead to larger V_{OC} loss and *FF* loss in the tandem solar cell due to the electrical power

loss. It is noted that the photocurrent of the tandem solar cell is smaller than the un-filtered Si bottom-cell and opaque PSC. This smaller photocurrent can mitigate the electrical loss and give more room for the trade-off between parasitic absorption and electrical losses.

5.4. Power Loss Due to Current Mismatch

Current matching between the top-cell and the bottom-cell is an important requirement for monolithically-integrated tandem solar cells because the photocurrent is determined by the smaller photocurrent of the two sub-cells; any current mismatch will lead to a large power loss. Albrecht et al.[60] have reported 18.1%-PCE monolithically-integrated PSC/Si tandem solar cells, however, they found that the photocurrent from the PSC top-cell was 16.7 mA cm^{-2}, while the photocurrent from the bottom-cell was only 14.3 mA cm^{-2}.[102] As a result, the photocurrent for PSC/Si tandem solar cell was limited by the Si bottom-cell, which suppressed the overall PCE to 18.1%. In order to achieve current matching, one approach is to reduce the thickness of HOIP layer in the PSC top-cell. By optimizing the thickness of all the functional and HOIP layers, Albrecht et al.[102] demonstrated that a photocurrent density of 17.5 mA cm^{-2} could be achieved in a PSC/Si tandem solar cell. If *FF* of 75.3% and V_{OC} of 1.78 V, could be maintained, it would improve the PCE of their tandem solar cells from 18.1% to 23.5%. The second strategy is to introduce wider-bandgap HOIP layer to allow the transmission of more photons to the bottom-cell.

6. Conclusions and Outlook

In summary, the emerging PSCs based on HOIPs have proven to be excellent top-cells for the tandem solar cells. To date, highly efficient tandem solar cells based on PSCs with different configurations have been successfully fabricated. For mechanically-stacked tandem solar cells, the top-cell and the bottom-cell are fabricated independently, and each sub-cell can operate at its maximum power point, and the champion device demonstrated a PCE of 25.2% for a $MAPbI_3$/Si tandem solar cell. Optically-coupled tandem solar cells utilize a dichroic mirror to direct the short-wavelength light to the PSC top-cell and the long-wavelength light to the bottom-cell. A total PCE of as high as 28.0% for a $MAPbI_3$/Si optically-coupled tandem solar cell has been reported. In the future, developing wide-bandgap PSCs with high EQE and large V_{OC} is crucial for the optically-coupled tandem solar cells to achieve >30% PCE. Nevertheless, the high cost of the dichroic mirror and the device geometry may limit the practical application of spectral-splitting tandem solar cells. Monolithically-integrated PSC/Si, PSC/CIGS, and PSC-1/PSC-2 tandem solar cells have been successfully demonstrated, with the best PCE as high as 23.6%. Current matching between top-cell and bottom-cell is important to avoid power loss in monolithically-integrated tandem solar cells. Compared to mechanically-stacked tandem solar cells, the monolithically-integrated tandem solar cells can reduce the electrode parasitic absorption due to the reduced number of transparent electrodes. However, when spiro-OMeTAD is used as hole-transport layer, strong parasitic absorption is observed. In the future, it is important to use hole-transport layers with low parasitic absorption to minimize optical loss. The highest-PCE monolithically-integrated PSC/Si tandem solar cells is based on the bandgaps of 1.55/1.1 eV; if the bandgap of the PSC can be increased to 1.7–1.8 eV in the future, it can reduce the thermalization loss and further improve the PCE of monolithically-integrated tandem solar cells.

The LCOE of PSC module is calculated to be 3.5–4.9 US cents kW h^{-1} based on an efficiency of 12% and lifetime of 15 years,[108] which is only around one third of the cost of Si-based PV technologies (9.78–19.33 US cents kW h^{-1}).[109] Considering the PSC/Si tandem solar cells can significantly improve the PCE of traditional PV module, the tandem device can reduce the balance of system cost (such as shipment, installation, land usage, etc.) and generate cheaper electricity compared to traditional PV module. Besides improving the PCE of PSC/Si or PSC/CIGS tandem solar cells, more efforts should be put into increasing the lifetime of PSCs to achieve low LCOE for the future commercialization of PSC-based tandem solar cells. Since PSCs still have much lower lifetime than Si-based solar cells, the faster degradation of PSCs could drag down the PCE of the tandem devices to be even less than that of the single-junction Si-based solar cells after a period of operation. Therefore, enhancing the stability of PSCs should be as important, if not more important than, as increasing the tandem solar cells PCE to over 30%.

Acknowledgements

We thank the financial support from the Department of Energy (award no. DE-EE0006709), and the National Science Foundation (award nos. DMR-1305913 and OIA-1538893).

Received: October 30, 2016
Revised: January 2, 2017
Published online:

[1] http://www.nrel.gov/ncpv/images/efficiency_chart.jpg, accessed: April, 2016.
[2] C. H. Henry, *J. Appl. Phys.* **1980**, *51*, 4494.
[3] Z. J. Yu, M. Leilaeioun, Z. Holman, *Nat. Energy* **2016**, *1*, 16137.
[4] https://en.wikipedia.org/wiki/Growth_of_photovoltaics#Forecast, accessed: December, 2016.
[5] https://www.ise.fraunhofer.de, accessed: December, 2016.
[6] J. F. Geisz, D. J. Friedman, *Semicond. Sci. Tech.* **2002**, *17*, 769.
[7] N. N. Lal, T. P. White, K. R. Catchpole, *IEEE J. Photovolt.* **2014**, *4*, 1380.
[8] T. Soga, K. Baskar, T. Kato, T. Jimbo, M. Umeno, *J. Cryst. Growth.* **1997**, *174*, 579.
[9] K. Tanabe, K. Watanabe, Y. Arakawa, *Sci. Rep.* **2012**, *2*, 349.
[10] Y. Alaskar, S. Arafin, D. Wickramaratne, M. A. Zurbuchen, L. He, J. McKay, Q. Lin, M. S. Goorsky, R. K. Lake, K. L. Wang, *Adv. Funct. Mater.* **2014**, *24*, 6629.
[11] K. Tanabe, K. Watanabe, Y. Arakawa, *Sci. Rep.* **2012**, *2*, 349.
[12] W. S. Yang, J. H. Noh, N. J. Jeon, Y. C. Kim, S. Ryu, J. Seo, S. I. Seok, *Science* **2015**, *348*, 1234.
[13] H. P. Zhou, Q. Chen, G. Li, S. Luo, T. B. Song, H. S. Duan, Z. R. Hong, J. B. You, Y. S. Liu, Y. Yang, *Science* **2014**, *345*, 542.

[14] W. Chen, Y. Wu, Y. Yue, J. Liu, W. Zhang, X. Yang, H. Chen, E. Bi, I. Ashraful, M. Grätzel, L. Han, *Science* **2015**, *350*, 944.
[15] A. Kojima, K. Teshima, Y. Shirai, T. Miyasaka, *J. Am. Chem. Soc.* **2009**, *131*, 6050.
[16] J. Burschka, N. Pellet, S. J. Moon, R. Humphry-Baker, P. Gao, M. K. Nazeeruddin, M. Grätzel, *Nature* **2013**, *499*, 316.
[17] M. Z. Liu, M. B. Johnston, H. J. Snaith, *Nature* **2013**, *501*, 395.
[18] Q. Dong, Y. Fang, Y. Shao, P. Mulligan, J. Qiu, L. Cao, J. Huang, *Science* **2015**, *347*, 967.
[19] W.-J. Yin, T. Shi, Y. Yan, *Appl. Phys. Lett.* **2014**, *104*, 063903.
[20] Z. Xiao, Y. Yuan, Q. Wang, Y. Shao, Y. Bai, Y. Deng, Q. Dong, M. Hu, C. Bi, J. Huang, *Mater. Sci. Eng. R.* **2016**, *101*, 1.
[21] T. M. Brenner, D. A. Egger, L. Kronik, G. Hodes, D. Cahen, *Nature Rev. Mater.* **2016**, *1*, 15007.
[22] S. D. Stranks, G. E. Eperon, G. Grancini, C. Menelaou, M. J. Alcocer, T. Leijtens, L. M. Herz, A. Petrozza, H. J. Snaith, *Science* **2013**, *342*, 341.
[23] C. Wehrenfennig, G. E. Eperon, M. B. Johnston, H. J. Snaith, L. M. Herz, *Adv. Mater.* **2014**, *26*, 1584.
[24] Z. G. Xiao, Y. B. Yuan, Q. Wang, Y. C. Shao, Y. Bai, Y. H. Deng, Q. F. Dong, M. Hu, C. Bi, J. S. Huang, *Mater. Sci. Eng. R-Rep* **2016**, *101*, 1.
[25] M. A. Green, A. Ho-Baillie, H. J. Snaith, *Nat. Photonics* **2014**, *8*, 506.
[26] P.-Y. Chen, J. Qi, M. T. Klug, X. Dang, P. T. Hammond, A. M. Belcher, *Energy Environ. Sci.* **2014**, *7*, 3659.
[27] M. Xiao, F. Huang, W. Huang, Y. Dkhissi, Y. Zhu, J. Etheridge, A. Gray-Weale, U. Bach, Y.-B. Cheng, L. Spiccia, *Angew. Chem.* **2014**, *126*, 10056.
[28] J. H. Im, I. H. Jang, N. Pellet, M. Gräetzel, N. G. Park, *Nat. Nanotech.* **2014**, *9*, 927.
[29] N. J. Jeon, J. H. Noh, Y. C. Kim, W. S. Yang, S. Ryu, S. I. Seol, *Nat. Mater.* **2014**, *13*, 897.
[30] Z. Xiao, Q. Dong, C. Bi, Y. Shao, Y. Yuan, J. Huang, *Adv. Mater.* **2014**, *26*, 6503.
[31] Y. Deng, E. Peng, Y. Shao, Z. Xiao, Q. Dong, J. Huang, *Energy Environ. Sci.* **2015**, *8*, 1544.
[32] K. Hwang, Y.-S. Jung, Y.-J. Heo, F. H. Scholes, S. E. Watkins, J. Subbiah, D. J. Jones, D.-Y. Kim, D. Vak, *Adv. Mater.* **2015**, *27*, 1241.
[33] E. Edri, S. Kirmayer, D. Cahen, G. Hodes, *J. Phys. Chem. Lett.* **2013**, *4*, 897.
[34] Y. Ogomi, A. Morita, S. Tsukamoto, T. Saitho, N. Fujikawa, Q. Shen, T. Toyoda, K. Yoshino, S. S. Pandey, T. L. Ma, S. Hayase, *J. Phys. Chem. Lett.* **2014**, *5*, 1004.
[35] F. Hao, C. C. Stoumpos, D. H. Cao, R. P. H. Chang, M. G. Kanatzidis, *Nat. Photonics* **2014**, *8*, 489.
[36] J. W. Lee, D. J. Seol, A. N. Cho, N. G. Park, *Adv. Mater.* **2014**, *26*, 4991.
[37] I. Almansouri, A. Ho-Baillie, M. A. Green, *Jpn. J. Appl. Phys.* **2015**, *54*, 08KD04.
[38] Y. J. Jiang, I. Almansouri, S. J. Huang, T. Young, Y. Li, Y. Peng, Q. C. Hou, L. Spiccia, U. Bach, Y. B. Cheng, M. A. Green, A. Ho-Baillie, *J. Mater. Chem. C* **2016**, *4*, 5679.
[39] C. D. Bailie, M. G. Christoforo, J. P. Mailoa, A. R. Bowring, E. L. Unger, W. H. Nguyen, J. Burschka, N. Pellet, J. Z. Lee, M. Grätzel, R. Noufi, T. Buonassisi, A. Salleo, M. D. McGehee, *Energy Environ. Sci.* **2015**, *8*, 956.
[40] P. Loper, S.-J. Moon, S. M. de Nicolas, B. Niesen, M. Ledinsky, S. Nicolay, J. Bailat, J.-H. Yum, S. De Wolf, C. Ballif, *Phys. Chem. Chem. Phys.* **2015**, *17*, 1619.
[41] J. Werner, G. Dubuis, A. Walter, P. Loeper, S.-J. Moon, S. Nicolay, M. Morales-Masis, S. De Wolf, B. Niesen, C. Ballif, *Sol. Energ. Mat. Sol. Cells* **2015**, *141*, 407.
[42] Y. Yang, Q. Chen, Y.-T. Hsieh, T.-B. Song, N. De Marco, H. Zhou, *ACS Nano* **2015**, *9*, 7714.
[43] L. Kranz, A. Abate, T. Feurer, F. Fu, E. Avancini, J. Loeckinger, P. Reinhard, S. M. Zakeeruddin, M. Grätzel, S. Buecheler, A. N. Tiwari, *J. Phys. Chem. Lett.* **2015**, *6*, 2676.
[44] F. Lang, M. A. Gluba, S. Albrecht, J. Rappich, L. Korte, B. Rech, N. H. Nickel, *J. Phys. Chem. Lett.* **2015**, *6*, 2745.
[45] J. Werner, S.-J. Moon, P. Löper, A. Walter, M. Filipic, C.-H. Weng, L. Löfgren, J. Bailat, M. Topic, M. M. Masis, R. Peibst, R. Brendel, S. Nicolay, S. D. Wolf, B. Niesen, C. Ballif, *31st European PV Solar Conference and Exhibition*, **2015**, Hamburg, Germany.
[46] F. Fu, T. Feurer, T. Jaeger, E. Avancini, B. Bissig, S. Yoon, S. Buecheler, A. N. Tiwari, *Nat. Commun.* **2015**, *6*, 8932.
[47] D. P. McMeekin, G. Sadoughi, W. Rehman, G. E. Eperon, M. Saliba, M. T. Hoerantner, A. Haghighirad, N. Sakai, L. Korte, B. Rech, M. B. Johnston, L. M. Herz, H. J. Snaith, *Science* **2016**, *351*, 151.
[48] K. A. Bush, C. D. Bailie, Y. Chen, A. R. Bowring, W. Wang, W. Ma, T. Leijtens, F. Moghadam, M. D. McGehee, *Adv. Mater.* **2016**, *28*, 3937.
[49] T. Duong, N. Lal, D. Grant, D. Jacobs, P. Zheng, S. Rahman, H. Shen, M. Stocks, A. Blakers, K. Weber, T. P. White, K. R. Catchpole, *IEEE J. Photovolt.* **2016**, *6*, 679.
[50] B. Chen, Y. Bai, Z. Yu, T. Li, X. Zheng, Q. F. Dong, L. She, M. Boccard, A. Gruverman, Z. Holman, J. S. Huang, *Adv. Energy Mater.* **2016**, *6*, 1601128.
[51] J. Werner, L. Barraud, A. Walter, M. Bräuninger, F. Sahli, D. Sacchetto, N. Tétreault, B. Paviet-Salomon, S.-J. Moon, C. Allebé, *ACS Energy Lett.* **2016**, *1*, 474.
[52] Z. Yang, A. Rajagopal, C. C. Chueh, S. B. Jo, B. Liu, T. Zhao, A. K. Y. Jen, *Adv. Mater.* **2016**, *28*, 8990.
[53] G. E. Eperon, T. Leijtens, K. A. Bush, T. Green, J. T.-W. Wang, D. P. McMeekin, G. Volonakis, R. L. Milot, D. J. Slotcavage, R. Belisle, *Science* **2016**, *354*, 861.
[54] F. Hao, C. C. Stoumpos, R. P. H. Chang, M. G. Kanatzidis, *J. Am. Chem. Soc.* **2014**, *136*, 8094.
[55] C. D. Bailie, M. D. McGehee, *MRS Bulletin* **2015**, *40*, 681.
[56] H. Uzu, M. Ichikawa, M. Hino, K. Nakano, T. Meguro, J. L. Hernandez, H.-S. Kim, N.-G. Park, K. Yamamoto, *Appl. Phys. Lett.* **2015**, *106*, 013506.
[57] R. Sheng, A. Ho-Baillie, S. J. Huang, M. Keevers, X. J. Hao, L. C. Jiang, Y. B. Cheng, M. A. Green, *J. Phys. Chem. Lett.* **2015**, *6*, 3931.
[58] T. Kinoshita, K. Nonomura, N. J. Jeon, F. Giordano, A. Abate, S. Uchida, T. Kubo, S. I. Seok, M. K. Nazeeruddin, A. Hagfeldt, M. Grätzel, H. Segawa, *Nat. Commun.* **2015**, *6*, 8834.
[59] J. P. Mailoa, C. D. Bailie, E. C. Johlin, E. T. Hoke, A. J. Akey, W. H. Nguyen, M. D. McGehee, T. Buonassisi, *Appl. Phys. Lett.* **2015**, *106*, 121105.
[60] S. Albrecht, M. Saliba, J. P. C. Baena, F. Lang, L. Kegelmann, M. Mews, L. Steier, A. Abate, J. Rappich, L. Korte, R. Schlatmann, M. K. Nazeeruddin, A. Hagfeldt, M. Grätzel, B. Rech, *Energy Environ. Sci.* **2016**, *9*, 81.
[61] J. Werner, C.-H. Weng, A. Walter, L. Fesquet, J. P. Seif, S. De Wolf, B. Niesen, C. Ballif, *J. Phys. Chem. Lett.* **2016**, *7*, 161.
[62] T. Todorov, T. Gershon, O. Gunawan, C. Sturdevant, S. Guha, *Appl. Phys. Lett.* **2014**, *105*, 173902.
[63] T. Todorov, T. Gershon, O. Gunawan, Y. S. Lee, C. Sturdevant, L.-Y. Chang, S. Guha, *Adv. Energy Mater.* **2015**, *5*, 1500799.
[64] J. H. Heo, J. H. Im, *Adv. Mater.* **2016**, *28*, 5121.
[65] C.-C. Chen, S.-H. Bae, W.-H. Chang, Z. Hong, G. Li, Q. Chen, H. Zhou, Y. Yang, *Mater. Horiz.* **2015**, *2*, 203.

[66] Y. Liu, L. A. Renna, M. Bag, Z. A. Page, P. Kim, J. Choi, T. Emrick, D. Venkataraman, T. P. Russell, *ACS Appl. Mater. Interfaces* **2016**, *8*, 7070.
[67] G. Y. Margulis, M. G. Christoforo, D. Lam, Z. M. Beiley, A. R. Bowring, C. D. Bailie, A. Salleo, M. D. McGehee, *Adv. Energy Mater.* **2013**, *3*, 1657.
[68] D. Shin, T. Kim, B. T. Ahn, S. M. Han, *ACS Appl. Mater. Interfaces* **2015**, *7*, 13557.
[69] F. Guo, P. Kubis, T. Przybilla, E. Spiecker, A. Hollmann, S. Langner, K. Forberich, C. J. Brabec, *Adv. Energy Mater.* **2015**, *5*, 1401779.
[70] D. Angmo, T. R. Andersen, J. J. Bentzen, M. Helgesen, R. R. Sondergaard, M. Jorgensen, J. E. Carle, E. Bundgaard, F. C. Krebs, *Adv. Funct. Mater.* **2015**, *25*, 4539.
[71] X. K. Li, Y. Jung, J. S. Huang, T. Goh, A. D. Taylor, *Adv. Energy Mater.* **2014**, *4*, 1400186.
[72] M. Lee, Y. Ko, B. K. Min, Y. Jun, *ChemSusChem* **2016**, *9*, 31.
[73] F. Guo, H. Azimi, Y. Hou, T. Przybilla, M. Y. Hu, C. Bronnbauer, S. Langner, E. Spiecker, K. Forberich, C. J. Brabec, *Nanoscale* **2015**, *7*, 1642.
[74] C. Y. Chang, K. T. Lee, W. K. Huang, H. Y. Siao, Y. C. Chang, *Chem. Mater.* **2015**, *27*, 5122.
[75] S. Nam, M. Song, D. H. Kim, B. Cho, H. M. Lee, J. D. Kwon, S. G. Park, K. S. Nam, Y. Jeong, S. H. Kwon, Y. C. Park, S. H. Jin, J. W. Kang, S. Jo, C. S. Kim, *Sci. Rep.* **2014**, *4*, 4788.
[76] J. J. Zhao, X. P. Zheng, Y. H. Deng, T. Li, Y. C. Shao, A. Gruverman, J. Shield, J. S. Huang, *Energy Environ. Sci.* **2016**, *9*, 3650.
[77] Z. C. Holman, A. Descoeudres, S. De Wolf, C. Ballif, *IEEE J. Photovolt.* **2013**, *3*, 1243.
[78] M. Morales-Masis, S. M. De Nicolas, J. Holovsky, S. De Wolf, C. Ballif, *IEEE J. Photovolt.* **2015**, *5*, 1340.
[79] G. E. Eperon, V. M. Burlakov, A. Goriely, H. J. Snaith, *ACS Nano* **2014**, *8*, 591.
[80] G. E. Eperon, D. Bryant, J. Troughton, S. D. Stranks, M. B. Johnston, T. Watson, D. A. Worsley, H. J. Snaith, *J. Phys. Chem. Lett.* **2015**, *6*, 129.
[81] E. Della Gaspera, Y. Peng, Q. Hou, L. Spiccia, U. Bach, J. J. Jasieniak, Y.-B. Cheng, *Nano Energy* **2015**, *13*, 249.
[82] P. You, Z. Liu, Q. Tai, S. Liu, F. Yan, *Adv. Mater.* **2015**, *27*, 3632.
[83] Z. Li, S. A. Kulkarni, P. P. Boix, E. Shi, A. Cao, K. Fu, S. K. Batabyal, J. Zhang, Q. Xiong, L. H. Wong, N. Mathews, S. G. Mhaisalkar, *ACS Nano* **2014**, *8*, 6797.
[84] F. Jiang, T. Liu, S. Zeng, Q. Zhao, X. Min, Z. Li, J. Tong, W. Meng, S. Xiong, Y. Zhou, *Opt. Express* **2015**, *23*, A83.
[85] D. Bryant, P. Greenwood, J. Troughton, M. Wijdekop, M. Carnie, M. Davies, K. Wojciechowski, H. J. Snaith, T. Watson, D. Worsley, *Adv. Mater.* **2014**, *26*, 7499.
[86] J. H. Noh, S. H. Im, J. H. Heo, T. N. Mandal, S. I. Seok, *Nano Lett.* **2013**, *13*, 1764.
[87] C. Bi, Y. B. Yuan, Y. J. Fang, J. S. Huang, *Adv. Energy Mater.* **2015**, *5*, 1401616.
[88] Y. X. Zhao, K. Zhu, *J. Am. Chem. Soc.* **2014**, *136*, 12241.
[89] M. Hu, C. Bi, Y. B. Yuan, Y. Bai, J. S. Huang, *Sci. Adv.* **2016**, *3*, 1500301.
[90] Y. Y. Zhou, M. J. Yang, O. S. Game, W. W. Wu, J. Kwun, M. A. Strauss, Y. F. Yan, J. S. Huang, K. Zhu, N. P. Padture, *ACS Appl. Mater. Interfaces* **2016**, *8*, 2232.
[91] G. E. Eperon, S. D. Stranks, C. Menelaou, M. B. Johnston, L. M. Herz, H. J. Snaith, *Energy Environ. Sci.* **2014**, *7*, 982.
[92] R. E. Beal, D. J. Slotcavage, T. Leijtens, A. R. Bowring, R. A. Belisle, W. H. Nguyen, G. F. Burkhard, E. T. Hoke, M. D. McGehee, *J. Phys. Chem. Lett.* **2016**, *7*, 746.
[93] B. W. Park, B. Philippe, X. L. Zhang, H. Rensmo, G. Boschloo, E. M. J. Johansson, *Adv. Mater.* **2015**, *27*, 6806.
[94] A. H. Slavney, T. Hu, A. M. Lindenberg, H. I. Karunadasa, *J. Am. Chem. Soc.* **2016**, *138*, 2138.
[95] G. E. Eperon, G. M. Paternò, R. J. Sutton, A. Zampetti, A. A. Haghighirad, F. Cacialli, H. J. Snaith, *J. Mater. Chem. A* **2015**, *3*, 19688.
[96] A. Swarnkar, A. R. Marshall, E. M. Sanehira, B. D. Chernomordik, D. T. Moore, J. A. Christians, T. Chakrabarti, J. M. Luther, *Science* **2016**, *354*, 92.
[97] W. D. Zhu, C. X. Bao, F. M. Li, X. X. Zhou, J. Yang, T. Yu, Z. G. Zou, *Chem. Commun.* **2016**, *52*, 304.
[98] E. T. Hoke, D. J. Slotcavage, E. R. Dohner, A. R. Bowring, H. I. Karunadasa, M. D. McGehee, *Chem. Sci.* **2015**, *6*, 613.
[99] C. Bi, Q. Wang, Y. Shao, Y. Yuan, Z. Xiao, J. Huang, *Nat. Commun.* **2015**, *6*, 7747.
[100] M. Hu, C. Bi, Y. Yuan, Y. Bai, J. Huang, *Adv. Sci.* **2016**, *3*, 1500301.
[101] Y. C. Shao, Y. J. Fang, T. Li, Q. Wang, Q. F. Dong, Y. H. Deng, Y. B. Yuan, H. T. Wei, M. Y. Wang, A. Gruverman, J. Shielda, J. S. Huang, *Energy Environ. Sci.* **2016**, *9*, 1752.
[102] S. Albrecht, M. Saliba, J. P. Correa-Baena, K. Jäger, L. Korte, A. Hagfeldt, M. Grätzel, B. Rech, *J. Opt.* **2016**, *18*, 064012.
[103] B. W. Schneider, N. N. Lal, S. Baker-Finch, T. P. White, *Opt. Express* **2014**, *22*, A1422.
[104] D. Shi, Y. Zeng, W. Shen, *Sci. Rep.* **2015**, *5*, 16504.
[105] B. Dudem, J. H. Heo, J. W. Leem, J. S. Yu, S. H. Im, *J. Mater. Chem. A* **2016**, *4*, 7573.
[106] J. P. Mailoa, C. D. Bailie, A. J. Akey, E. T. Hoke, E. C. Johlin, W. H. Nguyen, S. E. Sofia, M. D. McGehee, T. Buonassisi, in *2015 IEEE 42nd Photovoltaic Specialist Conference*, New Orleans, **2015**.
[107] D. L. Meier, D. K. Schroder, *IEEE Trans. Electron Dev* **1984**, *31*, 647.
[108] M. Cai, Y. Wu, H. Chen, X. Yang, Y. Qiang, L. Han, *Adv. Sci.* **2017**, *4*, 1600269.
[109] *Levelized Cost and Levelized Avoided Cost of New Generation Resources in the Annual Energy Outlook*, U.S. Energy Information Administration, **2015**.